



# Approaching the Ultimate Limit in Measurement Precision with RASER NMR

Simon Fleischer<sup>1,3</sup> · Sören Lehmkuhl<sup>2</sup> · Lars Lohmann<sup>3</sup> · Stephan Appelt<sup>1,3</sup>

Received: 7 July 2023 / Revised: 3 August 2023 / Accepted: 7 August 2023

© The Author(s) 2023

## Abstract

Radio-frequency Amplification by Stimulated Emission of Radiation (RASER) is a promising tool to study nonlinear phenomena or measure NMR parameters with unprecedented precision. Magnetic fields,  $J$ -couplings, and chemical shifts can be recorded over long periods of time without the need for radiofrequency excitation and signal averaging. One key feature of RASER NMR spectroscopy is the improvement in precision, which grows with the measurement time  $T_m^{3/2}$ , unlike conventional NMR spectroscopy, where the precision increases with  $T_m^{1/2}$ . However, when detecting NMR signals over minutes to hours, using available NMR magnets (ppb homogeneity), the achieved frequency resolution will eventually be limited by magnetic field fluctuations. Here, we demonstrate that full compensation is possible even for open low-field electromagnets, where magnetic field fluctuations are intrinsically present (in the ppm regime). A prerequisite for compensation is that the spectrum contains at least one isolated RASER line to be used as a reference, and the sample experiences exclusively common magnetic field fluctuations, that is, ones that are equal over the entire sample volume. We discuss the current limits of precision for RASER NMR measurements for two different cases: The single-compartment RASER involving  $J$ -coupled modes, and the two-compartment RASER involving chemically shifted species. In the first case, the limit of measurable difference approaches the Cramér-Rao lower bound (CRLB), achieving a measurement precision  $\sigma_f < 10^{-4}$  Hz. In the second case, the measured chemical shift separation is plagued by independently fluctuating distant dipolar fields (DDF). The measured independent field fluctuation between the two chambers is in the order of tens of mHz. In both cases, new limits of precision are achieved, which paves the way for sub-mHz detection of NMR parameters, rotational rates, and non-linear phenomena such as chaos and synchrony.

---

Extended author information available on the last page of the article

## 1 Introduction

The precision of NMR spectroscopy is limited by the signal-to-noise ratio (SNR). To increase the SNR, hyperpolarized magnetic resonance (MR) allows to generate high nuclear spin polarization in the solid, liquid and gas phase, boosting MR sensitivity by several orders of magnitude. The most prominent hyperpolarization techniques rely on Dynamic Nuclear Polarization (DNP) [1–4], Spin Exchange Optical Pumping (SEOP) [5–8], metastability exchange optical pumping (MEOP) [9] and parahydrogen ( $p$ -H<sub>2</sub>)-based approaches. The latter can be divided into Para-Hydrogen Induced Polarization (PHIP) [10–14] and Signal Amplification By Reversible Exchange (SABRE) [15–19]. PHIP is based on polarization transfer by incorporating the polarized hydrogen into the substrate molecule by hydrogenation, allowing for especially high degrees of polarization [10–12]. SABRE is an efficient way to continuously pump a liquid state RASER at room temperature and over a wide range of magnetic fields [15, 18, 20]. In SABRE,  $p$ -H<sub>2</sub> and the target substrate reversibly coordinate to a metal–organic catalyst with a system-specific contact time. During this time, the singlet state of  $p$ -H<sub>2</sub> is transferred and converted via  $J$ -coupling into a highly polarized state of the target nuclei [15, 16].

Since the magnetization created by most hyperpolarization schemes is field-independent, the SNR of NMR signals depends only weakly on the static magnetic field  $B_0$ . Thus, hyperpolarization is especially advantageous for low-field NMR, using unshielded electromagnets in the 10 mT regime or compact Halbach magnets in the 1 T regime. Both electromagnets and Halbach magnets are often plagued by slow magnetic field drifts, which can be accounted for by using an independent reference line close to the sample location.

Another factor that limits the precision of an NMR experiment is the spectral linewidth, given by  $1/(\pi T_2^*)$ . This limit, given by the transverse relaxation rate  $1/T_2^*$ , can be overcome by introducing a negative damping, or a negative spin temperature, which prolongs the transverse relaxation time. For a spin 1/2 species, the negative spin temperature is equivalent to an equilibrium population inversion  $d_0 = N_2 - N_1$  between the upper and lower Zeeman levels 2 and 1. If  $d_0 = N_2 - N_1$  is high enough, such that the total damping becomes negative (the threshold condition is met), RASER action starts, generating an oscillating signal of arbitrary length. Hyperpolarization can create sufficiently high population inversion for maintaining RASER action over an extended period of time. Nuclear spin-based RASERS operating in the gas- [21–23], liquid- [24–29] and solid-phase [30–34] have been demonstrated in recent years.

The first  $p$ -H<sub>2</sub>-pumped <sup>1</sup>H RASER has demonstrated a substantial increase in the precision of  $J$ -coupled Nuclear Magnetic Resonance (NMR) spectroscopy [35]. Subsequent work on SABRE and PHIP pumped <sup>1</sup>H RASERS at both high and low magnetic fields has paved the way for high-resolution NMR spectroscopy, with possible applications for NMR gyroscopes and magnetometry. Membrane-mediated RASER pumping (using tube-in-tube reactors), RASER-induced multinuclear signal enhancement, <sup>13</sup>C RASER action during a chemical transformation and RASER MRI [20, 28, 29, 35–40] were recently demonstrated.

Our contribution to this Special Issue of *Applied Magnetic Resonance* is devoted to high-precision RASER NMR spectroscopy. In general, an increase in precision in every measurement technology leads to fundamental advances in understanding the basic laws of nature, or to technological breakthroughs. One prominent example is the huge improvement in the precision of laser-interferometry, which recently led to the first direct observation of gravitational waves. Another example is the high precision of GPS, which, along with the development of low-cost mobile phones, has led to mass applications in civil navigation. A similar development is expected in the next decade for RASER NMR spectroscopy, with an increase in precision for the measurement of molecular parameters, mechanical rotations or of non-linear phenomena.

Here, we demonstrate how to measure  $J$ -couplings and chemical shift differences with a precision in the sub-mHz range, with low hardware requirements. This includes open, unshielded electromagnets (several 10 mT) combined with low-cost External High Quality-factor Enhancement (EHQE) resonators [41], or alternatively compact Halbach magnets, employing  $p$ -H<sub>2</sub>-based hyperpolarization schemes. The detriment of long-term frequency drifts can be alleviated with proper magnetic field correction schemes. This allows for the on-line detection of very small changes in molecular parameters.

## 2 General Theory of a Two-Mode RASER

First, we will discuss the general case of two different RASER modes with a common transverse relaxation rate  $1/T_2^*$ . The coupling between the low-frequency photons and the nuclear spins is given by the coupling constant  $\beta = |gg^*|/\kappa = \mu_0 \hbar \gamma_H^2 \eta Q / (4V_s)$ , where  $g$  is the coupling strength and  $\kappa = \omega_0/Q$  is the damping rate of the LC-resonator, with a quality factor  $Q$  and operating at angular frequency  $\omega_0$ . The constants  $\mu_0, \hbar, \gamma_H$  denote the vacuum permeability, the reduced Planck's constant, and the proton gyromagnetic ratio, respectively. The sample volume is denoted by  $V_s$ , and  $\eta$  is the filling factor. We assume the general case of two different compartments with two different RASER modes. Different longitudinal relaxation rates are denoted as  $1/T_1^{(1)}$  and  $1/T_1^{(2)}$ . In a realistic scenario of two independently pumped compartments, the pumping rates  $\Gamma_i(t)$ ,  $i=1, 2$  can differ in magnitude and display independent fluctuations, such that  $\Gamma_i(t) = \Gamma_i [1 + f_i(t)]$ , where  $\Gamma_i$  is the average pumping rate and  $f_i(t)$  is a random function, the residual mean square (rms) value of which lies in the range of 0.01–0.2. In total, the RASER equations are described by six coupled differential equations for the two population inversions  $d_i$ , the transverse spin components  $A_i$ , and the phases  $\phi_i$

$$\dot{d}_1 = \Gamma_1(t)[d_{1,0} - d_1] - \frac{d_1}{T_1^{(1)}} - 4\beta \sum_{j,k=1}^2 A_j A_k \cos(\phi_j - \phi_k), \tag{1}$$

$$\dot{A}_1 = \left[ \beta d_1 - \frac{1}{T_2^*} \right] A_1 + \beta d_1 A_2 \cos(\phi_2 - \phi_1), \tag{2}$$

$$\dot{\phi}_1 = \omega_1 + \beta d_1 \frac{A_2}{A_1} \sin(\phi_2 - \phi_1), \quad (3)$$

$$\dot{d}_2 = \Gamma_2(t)[d_{2,0} - d_2] - \frac{d_2}{T_1^{(2)}} - 4\beta \sum_{j,k=1}^2 A_j A_k \cos(\phi_j - \phi_k), \quad (4)$$

$$\dot{A}_2 = \left[ \beta d_2 - \frac{1}{T_2^*} \right] A_2 + \beta d_2 A_1 \cos(\phi_2 - \phi_1), \quad (5)$$

$$\dot{\phi}_2 = \omega_2 - \beta d_2 \frac{A_1}{A_2} \sin(\phi_2 - \phi_1). \quad (6)$$

The two different angular frequencies of the independently pumped compartments are denoted by  $\omega_1$  and by  $\omega_2$ . The specific form of the angular frequencies  $\omega_1$  and  $\omega_2$  depends on whether a gradient-controlled two-compartment RASER or a single-compartment RASER with two  $J$ -coupled angular frequencies is investigated.

## 2.1 Two $J$ -coupled RASER Modes in a Single Compartment

The interaction between two nonlinearly coupled RASER modes can be studied in different ways. Here, we begin with the simple case of one compartment without a magnetic field gradient  $G_z=0$  and one RASER species (zero chemical shift difference, see Fig. 1a). We assume that the RASER is oscillating at two distinct angular frequencies  $\omega_2 - \omega_1 = 2\pi J$ . This frequency difference is caused by  $J$ -coupling-induced splitting of two different spin states, as well as small additional non-linear shifts, which are also accounted for by the parameter  $J$ . A RASER with such a splitting has been shown for two specific spin states in  $^{15}\text{N}$ -pyridine with  $J=0.7$  Hz [35]. For simplicity, the population inversions and transverse spin components, presented in the general theory, Eqs. (1–6), are assumed to be the same for both states, i.e.  $d_1=d_2=d$ ,  $d_{1,0}=d_{2,0}=d_0$  and  $A_1=A_2=A$ . We assume a common pumping rate with small fluctuations for both modes, i.e.  $\Gamma_1(t) = \Gamma_2(t) = \Gamma_0[1 + f(t)]$  with  $|f(t)| < 1$ . Both  $J$ -coupled modes fluctuate exactly by the same amount, so the total magnetic field including fluctuations is  $\gamma_H[B_0(1 + \Delta) + \delta B(t)]$ , where  $\Delta$  is the common chemical shift value for both  $J$ -coupled spin states. Introducing the phase difference  $\Psi(t) = \phi_2(t) - \phi_1(t)$ , the six differential equations in Eqs. (1–6) can be simplified to a system of three coupled differential equations for the variables  $d$ ,  $A$  and  $\Psi$ , which are

$$\dot{d} = \Gamma_0[1 + f(t)][d_0 - d(t)] - \frac{d}{T_1} - 8\beta A^2[1 + \cos \Psi], \quad (7)$$

$$\dot{A} = \left[ \beta d(t)(1 + \cos \Psi) - \frac{1}{T_2^*} \right] A, \quad (8)$$

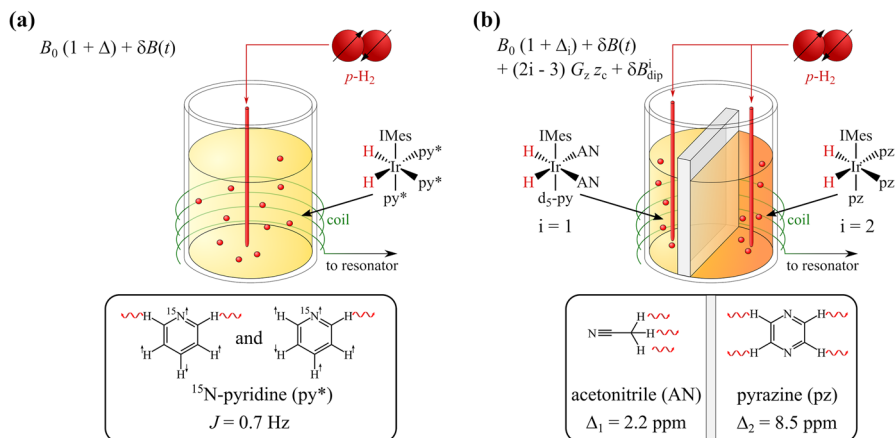


**Fig. 1** The continuously SABRE-pumped single-compartment  $^1\text{H}$  RASER operating with  $^{15}\text{N}$ -pyridine ( $\text{py}^*$ ) is shown in **a**. The origin of the two RASER lines of  $\text{py}^*$  is due to  $J = 0.7 \text{ Hz}$  coupling. This net coupling results from a combination of two spin-flips, with the individual couplings  $J_{24} - J_{25} + 0.5 J_{26} = 0.69 \text{ Hz}$ , with  $J_{24} = 1.78 \text{ Hz}$ ,  $J_{25} = 0.96 \text{ Hz}$ ,  $J_{26} = 0.13 \text{ Hz}$ . See [35:SI] for details. The chemical shift  $\Delta$  is exactly the same for both  $^{15}\text{N}$ -pyridine spin-states. The average common magnetic field in the single-compartment RASER is  $B_0(1 + \Delta)\delta B(t)$ . After elimination of the common field fluctuations  $\delta B(t)$ , the precision for determining the  $J$ -coupling should only be limited by the Cramér-Rao lower bound (see Sect. 2.3 for a detailed discussion). **b**: Two-compartment RASER for two separately SABRE-pumped chemical species acetonitrile (AN) and pyrazine (pz).  $\text{d}_5$ -pyridine ( $\text{d}_5\text{-py}$ ) is added to the compartment containing AN in order to stabilize the catalytic species. The corresponding chemical shifts are  $\Delta_1 = 2.2 \text{ ppm}$  (AN) and  $\Delta_2 = 8.5 \text{ ppm}$  (pz), respectively. The continuous parahydrogen ( $p\text{-H}_2$ ) supply through the injection capillaries delivers  $p\text{-H}_2$  bubbles, which induce a fast, irregular motion in the liquid sample in both compartments ( $\text{d}_5$ -methanol + substrate + catalyst). The chemical shift difference at  $166.6 \text{ kHz}$   $^1\text{H}$  resonance frequency ( $B_0 = 3.91 \text{ mT}$ ) is  $(\gamma_{\text{H}}/2\pi)B_0(\Delta_2 - \Delta_1) = 1.05 \text{ Hz}$ . For both cases (**a**) and (**b**), relevant average magnetic fields, including common magnetic field fluctuations  $\delta B(t)$  and individual distant dipolar fields  $\delta B_{\text{dip}}^i(t)$ , are given on the top

$$\dot{\Psi} = \dot{\phi}_2 - \dot{\phi}_1 = 2\pi J + 2\beta d(t) \sin \Psi. \quad (9)$$

Different effects can be responsible for variations in the observed splitting. The first effect is cavity pulling, which shifts each  $J$ -coupled line by a different amount towards the central cavity frequency, depending on the respective off-resonance [42–44]. The estimated shift due to cavity pulling is smaller than  $1 \text{ mHz}$  as will be shown in Sect. 3.3. The second effect is a non-linear phenomenon caused by the term  $2\beta d \sin \Psi$  in Eq. (9). This non-linear effect, which has been reported recently [44], leads to a decrease in the observed  $J$ -coupling-induced splitting depending on the ratio of the amount of splitting due to  $J$ -coupling and the size of the radiation-damping term  $\beta d/\pi$ . Simulations based on Eqs. (7–9) show that for our experimental conditions these effects can be in the order of  $10\text{--}30 \text{ mHz}$ , which can be detected experimentally with RASER spectroscopy. The third effect is a fluctuation in the pumping rate  $\Gamma_0[1 + f(t)]$ . This fluctuation is related to corresponding changes in the population inversion  $d(t)$ , and consequently to a slight broadening and a shift of each

RASER line, through Eqs. (7–9). Whether or not the extent of this type of non-linear shift is relevant in the mHz regime is not yet known, and warrants future investigations. Finally, slow fluctuations and drifts of the  $J$ -coupling constant itself caused by changes in solvent temperature and substrate concentration (e.g. due to evaporation of the solvent) are possible. A higher substrate concentration could change the  $J$ -coupling constant by modified intermolecular interactions. Whether this is competing with the non-linear shifts in the 10 mHz regime is an open question.

## 2.2 The Gradient Controlled, Chemically Shifted Two-Compartment RASER

In this section, we consider the gradient-controlled, two-compartment RASER, where each compartment contains a different chemical species, with chemical shift  $\Delta_2$  and  $\Delta_1$  (see Fig. 1b). The two compartments are pumped independently, with the pumping rates  $\Gamma_i [1 + f_i(t)]$ ,  $i=1,2$ , where  $\Gamma_i$  is a constant pumping rate and  $\Gamma_i f_i(t)$  denotes slow fluctuations in the order of 10% of the rate  $\Gamma_i$ . We assume simultaneous RASER action of the two chemical species  $\Delta_i$ , provided the angular frequency difference  $\omega_2 - \omega_1 = \gamma_H B_0 (\Delta_2 - \Delta_1)$  is sufficiently large. The angular Larmor frequency in the static field  $B_0$  (typically a few mT) is  $\gamma_H B_0$ , and  $\gamma_H = 2\pi \times 4.256$  kHz/G is the proton gyromagnetic ratio. Besides the chemical shift difference  $\gamma_H B_0 (\Delta_2 - \Delta_1)$ , a magnetic field gradient  $G_z$  (in mG/cm) can be applied to cause a deliberate relative shift in the RASER angular frequencies in compartment  $i=1,2$ . As shown recently in [44], in the presence of fast random motion in each compartment, two different averaged RASER angular frequencies  $\omega_i = (2i - 3)\gamma_H G_z z_c$  can be observed, where  $(2i - 3)z_c$  are the individual centers of gravity of each compartment  $i=1,2$ . The combined action of the gradient  $G_z$  and the chemical shift difference  $\Delta_2 - \Delta_1$  controls the angular frequency separation between the two RASER modes. The additional degrees of freedom gained by this setup allow for a more in-depth investigation of the underlying phenomena.

One limiting factor for the precision of RASER NMR spectroscopy is the presence of magnetic field fluctuations  $\delta B$ . These fluctuations consist of common external field fluctuations, current fluctuations with respect to the  $B_0$  field coil, common distant dipolar fields (common DDF), and fluctuating non-common DDF fields, as well as frequency drifts of the reference oscillator. The total averaged DDF (common and non-common) in each compartment  $\langle B_{\text{dip}}^{(i)}(t) \rangle$ ,  $i=1,2$  is proportional to the population inversion  $d_i(t)$  according to

$$\left\langle B_{\text{dip}}^{(i)}(t) \right\rangle = \frac{\mu_0}{4V_s} \hbar \gamma_H \xi d_i(t), \quad \text{for } i = 1, 2 \quad (10)$$

where  $\mu_0$ ,  $\hbar$  and  $V_s$  denote the vacuum permeability, the reduced Planck's constant and the sample volume, respectively. The shape factor  $\xi$  is a function of the sample geometry, which can range from  $-1/2 \leq \xi \leq 1$ .  $\xi=0$  represents a perfect sphere,  $\xi=-1/2$  a long cylinder, and  $\xi=1$  a thin disc. Since in our case the shape of the two compartments approaches two long cylinders,  $\xi=-1/2$ , and non-common DDF fluctuations cannot be neglected. For a single RASER mode, the time-dependent response  $d_i(t)$  to the fluctuating pumping rates is a stationary value  $d_{\text{stat}}$ ,

superimposed by small fluctuations, while for a two-mode RASER the response contains stationary, oscillatory and random components. In general, the time-dependent response of  $d_i(t)$  and  $\langle B_{\text{dip}}^{(i)}(t) \rangle$  regarding the fluctuating pumping rates  $\Gamma_i[1+f_i(t)]$  can reach high complexity. At higher values of the equilibrium population inversions  $d_{i,0}$ , multiple period doubling, and even chaotic behavior of  $d_i(t)$  and of the transverse spin component  $A(t)$  is possible. The precise knowledge of the DDF and of  $d_i(t)$  might be important for the stability of multi-mode RASER operation. For example, the point of transition from chaos to a collapsed (synchronous) state is highly sensitive to fluctuations. Here, we assume the RASER to be in a stationary state with small fluctuations, and that the mode separation is large enough to avoid complex behavior. Under these conditions, the DDF in each compartment  $i=1,2$  can be subdivided into two parts, i.e.  $\langle B_{\text{dip}}^{(i)}(t) \rangle = B_{\text{dip}}^{\text{com}}(t) + \delta B_{\text{dip}}^{(i)}(t)$ , with the fluctuating common part  $B_{\text{dip}}^{\text{com}}(t)$  and the fluctuating independent parts in  $\delta B_{\text{dip}}^{(i)}(t)$ . If the common part  $B_{\text{dip}}^{\text{com}}(t)$  is incorporated into the magnetic field fluctuations  $\delta B$ , the total angular frequency in each compartment  $\omega_i$  can be written as

$$\omega_i = \gamma_H [B_0(1 + \Delta_i) + \delta B(t) + (2i - 3)G_z z_c] + \gamma_H \delta B_{\text{dip}}^{(i)} - \omega_{\text{of}}. \tag{11}$$

The offset angular frequency  $\omega_{\text{of}}$  is chosen close to the angular radio frequency (here:  $2\pi \times 166.6$  kHz) in order to obtain RASER spectra with off-resonance values in the order of about 10 Hz. Since the common frequency fluctuations in both compartments can be eliminated by a correction procedure (see Sect. 2.4), the angular frequency difference is given by  $\omega_2 - \omega_1 = \gamma_H [B_0(\Delta_2 - \Delta_1) + 2G_z z_c + \delta B_{\text{dip}}^{(2)}(t) - \delta B_{\text{dip}}^{(1)}(t)]$ . Therefore, the common field fluctuations  $\delta B(t)$  and the offset  $\omega_{\text{of}}$  cancel out, while small DDF fluctuations  $\delta B_{\text{dip}}^{(2)}(t) - \delta B_{\text{dip}}^{(1)}(t)$  and changes in the chemical shifts  $\Delta_1(t)$  and  $\Delta_2(t)$  remain. In the experimental Sect. 3.5, it will be shown that the major contribution to fluctuations in angular frequency is due to the term  $\gamma_H (\delta B_{\text{dip}}^{(2)}(t) - \delta B_{\text{dip}}^{(1)}(t))$ , which in our case is in the order of tens of mHz.

### 2.3 Cramér-Rao Lower Bound

The precision of a measured RASER NMR spectrum can be quantified using a theoretical lower bound which sets an ultimate limit for the measurement accuracy. This so-called Cramér-Rao lower bound (CRLB) is defined as the standard deviation in measurement precision  $\sigma_f$  in frequency space. For the case of an exponentially damped signal (a Lorentzian line in Fourier space), the CRLB [35:SI, 45] can be written as

$$\sigma_f = \frac{\sqrt{3}}{\pi \text{SNR} \sqrt{\text{BWT}_m^{3/2}}}. \tag{12}$$

The measurement precision  $\sigma_f$  in Eq. (12) improves with a signal-to-noise ratio (SNR), the band-width of detection (BW) in Hz and with the measurement time  $T_m$ , the last of which is defined by a window with exponentially damped flanks folded with the RASER signal (see Sect. 2.4). The reason for choosing this exponential window is to prove the validity of the CRLB in the form given by Eq. (12). For exponentially damped signals in the time domain the corresponding Fourier transformed line is a Lorentzian having a width  $w=2/(\pi T_m)$ . The essential feature of CRLB is the improvement in precision (the decrease in  $\sigma_f$ ) with the factor  $\propto 1/(T_m^{3/2})$ , which distinguishes RASER NMR spectroscopy from standard NMR spectroscopy. Given an integer number  $N$  of NMR measurements (each lasting about three times the transverse  $T_2$  relaxation times, over a total NMR measurement time  $T_m=N 3T_2$  the improvement in SNR and in measurement precision is  $\sigma_f \propto 1/T_m^{1/2}$ . This improvement scales less strongly compared to  $\sigma_f \propto 1/T_m^{3/2}$  valid for a RASER experiment. However,  $\sigma_f \propto 1/T_m^{3/2}$  for a RASER is only fulfilled as long as fluctuations of the  $J$ -coupling or of the chemical shift values are sufficiently small for long times  $T_m$ . We anticipate that in a realistic case, the improvement in precision for RASER NMR very closely approaches CRLB.

#### 2.4 A Correction Procedure for the Elimination of Common Fluctuating Magnetic Fields $\delta B(t)$

For long-lasting RASER signals in the order of several hundred seconds, common magnetic field fluctuations  $\delta B(t)$  pose the main limiting factor for precision RASER NMR spectroscopy. In the following, we describe a nine-step procedure for the compensation of  $\delta B(t)$  together with a visualization of the essential steps shown in Fig. 2. We assume a stationary RASER state, which oscillates at two distinct angular frequencies  $\nu_1$  and  $\nu_2$ , with some broadening due to common fluctuations. In the first step I, a section of the RASER signal with a length of  $5 T_m$  around a central time  $t_c$  is chosen. Figure 2a shows an example for a measured RASER signal slice with a duration of 100 s ( $T_m=20$  s) around  $t_c=350$  s. In step II, the RASER signal slice is Fourier transformed. The resulting spectrum with real and imaginary parts is characterized by two lines centered at frequencies  $\nu_1$  and  $\nu_2$  ( $\nu_1 < \nu_2$ ), which are broadened and distorted in a self-similar way due to common field fluctuations (Fig. 2b). We assume that the two peaks do not overlap. In step III, we isolate the peak at  $\nu_1$  by setting the real and imaginary part of the spectrum to 0 outside of the range  $[\nu_1 - 0.5 \cdot (\nu_2 - \nu_1), \nu_1 + 0.5 \cdot (\nu_2 - \nu_1)]$ , with the boundary condition  $0.5 \cdot (\nu_2 - \nu_1) < \nu_1$ . This results in a spectrum containing only the selected broadened peak at frequency  $\nu_1$ , while preserving its spectral shape with respect to the original spectrum. The spectrum is then shifted in frequency space by a few Hz (Fig. 2c) to avoid a peak at zero frequency in the final spectrum. In step IV, an inverse Fourier transform is performed on the isolated peak, which results in a signal in the time domain with real and imaginary part (Fig. 2d). In step V, the imaginary part is multiplied by  $(-1)$ , generating the conjugate complex signal in time with respect to the line shown in Fig. 2c. In step VI, the negative imaginary part is multiplied with the



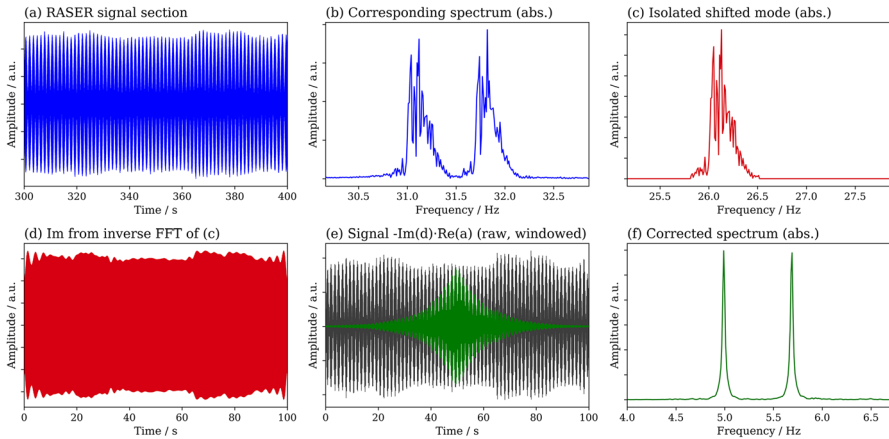


**Fig. 2** Visualization of the correction procedure for compensating common magnetic field fluctuations. **a** Raw two-mode RASER signal measured at time interval  $300\text{ s} < t < 400\text{ s}$ . **b** Corresponding spectrum showing two self-similar broadened lines. **c** The left peak in **b** is isolated and shifted in frequency space. **d** Imaginary part (Im) of the RASER signal obtained after inverse Fourier transformation of **c**. **e** The imaginary part (Im) of the RASER signal from **d** is first multiplied by  $(-1)$  and then multiplied by the real (Re) signal in **a**. The result (grey) is folded with an exponential window of duration  $T_m = 20\text{ s}$ , resulting in the signal shown in green. **f** The Fourier transformed spectrum of **(e, green)** is phased in the absolute mode. Two RASER lines can be identified, which are free of common magnetic field fluctuations

original real RASER signal, which results in an imaginary valued RASER signal  $R(t)$  (see Fig. 2e, grey). In step VII,  $R(t)$  is multiplied by an exponential window, the maximum amplitude of which lies at time  $t_c$ , and decays to  $1/e$  after the time  $T_m/2$  (Fig. 2e, green). The shape of this window, which is described by the function  $\exp\left[-\left|2(t-t_c)/T_m\right|\right]$ , is chosen in order to compare the results to the Cramér-Rao lower bound (CRLB, see Sect. 2.3). This results in a signal  $R(t) \exp\left[-\left|2(t-t_c)/T_m\right|\right]$ , which is then zero padded. In step VIII, the signal is Fourier transformed once more, resulting in a spectrum with real and imaginary parts. It is characterized by lines free of field fluctuations, but still displays the typical phase oscillations characteristic for RASER spectra (not shown in Fig. 2). In the last step IX, the spectrum is displayed in the absolute mode (see Fig. 2f) to avoid these phase oscillations. An analytical function given by  $\text{Abs}_j(\nu) = \sqrt{L_j^2(\nu) + D_j^2(\nu)}$  can be fitted to each of the two lines with index  $j=1,2$ . The Lorentzian and dispersion functions are given by  $L_j(\nu) = A_j \left\{ 1 + [2(\nu_j - \nu)/w_j]^2 \right\}^{-1}$  and  $D_j(\nu) = 2A_j(\nu_j - \nu)w_j^{-1} \left\{ 1 + [2(\nu_j - \nu)/w_j]^2 \right\}^{-1}$ , where  $A_j$ ,  $w_j$  and  $\nu_j$  for each line is the corresponding amplitude, linewidth (FWHM) and peak center frequency, respectively. From the fit of  $\text{Abs}_j(\nu)$  at each line for a given measurement time  $T_m$ , the standard deviation in measurement precision  $\sigma_f$  can be evaluated.

### 3 Experimental Results

#### 3.1 Two RASER Modes in One Compartment

We start with an analysis of the precision of RASER NMR spectroscopy for two  $J$ -coupled modes, which are oscillating in one single compartment. The results are quantified with respect to the measured precision in the line position, and compared to the CRLB. Figure 3a shows an example for a SABRE-pumped two-mode  $^1\text{H}$ -RASER from  $^{15}\text{N}$ -pyridine measured over 1200 s [35:SI]. The two spin states of  $^{15}\text{N}$ -pyridine indicated in Fig. 1a are the reason for the observed two modes. Figure 3b shows a time slice of 100 s of the corresponding beat signal of two RASER modes with nearly equal amplitude. The displayed signal is folded with an exponentially decreasing time window of  $T_m = 20$  s, which falls off in signal amplitude by  $1/e$  over a time  $T_m/2$  from the center at time  $t_c$ . This window is chosen to define a proper measurement time  $T_m$ , which can be compared to the CRLB, and to avoid sinc artifacts in the Fourier transformed spectrum. The spectrum in Fig. 3c, phased

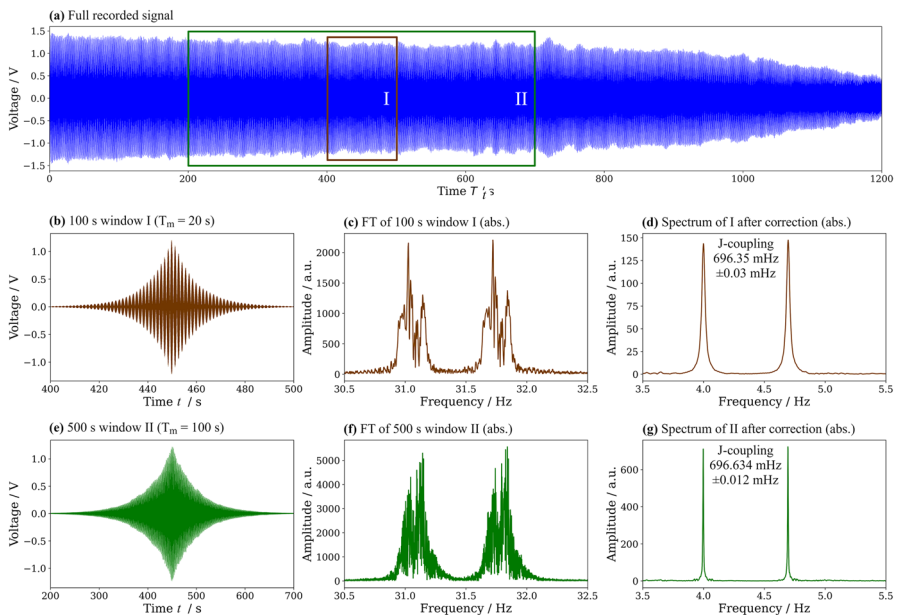


**Fig. 3** a SABRE pumped RASER signal of two  $J$ -coupled lines from  $^{15}\text{N}$ -pyridine measured over 1200 s. The two-mode RASER oscillations are measured in one compartment at 41.6 kHz ( $B_0 = 0.977$  mT). The slow decrease in RASER amplitude versus time is due to the evaporation of liquid  $d_4$ -methanol, which causes a decrease in the  $T_1$  relaxation time. (see simulation in Appendix). Two-time slices of 100 s (I) and 500 s (II) are folded by an exponential time window, decreasing by  $1/e$  after the measurement time  $T_m/2$  ( $T_m = 20$  s in **b** and 100 s in **e**). The corresponding uncorrected Fourier transformed signals (absolute mode) are shown in **c** and **f**. These spectra are characterized by self-similar broadened structures, which indicate common magnetic field fluctuations  $\delta B(t)$ . **d**, **g** show narrow peaks after the correction of field fluctuations. A fit through both peaks in **d**, **g** results in a value for the  $J$ -coupling of 696.1 mHz with an uncertainty in the precision of  $\pm 0.03$  mHz in **d** and  $\pm 0.012$  mHz in **g**, respectively

in the absolute mode, shows two broadened lines (width  $\sim 0.1$  Hz) and self-similar structures separated by  $J=0.7$  Hz. The two self-similar lines indicate the presence of common magnetic field fluctuations  $\delta B(t)$ . As shown in Fig. 3f, the line broadening is more severe for the longer measurement time  $T_m=100$  s (Fig. 3e), which is about 0.2 Hz at 41 kHz  $^1\text{H}$  resonance frequency. The observed broadening is consistent with typical slow  $B_0$ -field drifts of about 5 ppm on a time scale of 100 s. After correcting both spectra by removing magnetic field fluctuations  $\delta B(t)$  with the procedure detailed in Sect. 2.4, exactly two RASER lines remain. Their spectra are depicted in the absolute mode in Fig. 3d, g for  $T_m=20, 100$  s, respectively. This nearly perfect cancelling of common fluctuations is possible in this case, since the two lines are measured in one compartment, where both  $J$ -coupled lines experience the same common field fluctuations. So, we expect to closely approach the CRLB, as long as line broadening due to drifts of the  $J$ -coupling is much smaller than the field fluctuations. A numerical expression of the CRLB versus the time  $T_m$  exists, provided the SNR and the bandwidth of detection (BW) are known (see Eq. 12). The RASER signal amplitude in Fig. 3a is 1 V at half height. The residual-mean-square (rms) baseline noise on the 100 ms scale (in the absence of a RASER signal) is about 20–30 mV (not shown in Fig. 3). Apart from this, slow fluctuations on the scale of 1–10 s exist after the RASER has started and reached a stationary state, with an rms amplitude in the order of 50 mV–150 mV. The combination of both noise sources corresponds to an estimated total signal-to-noise ratio of  $\text{SNR}=12$ . This observed SNR on a long time scale can be confirmed by simulations based on the RASER Eqs. (7–9), which includes a slow fluctuating pumping rate  $\Gamma_0[1+f(t)]$  where the rms value of the fluctuating part  $f(t)$  is on the order of 0.1 of the constant rate  $\Gamma_0$ . Given a measured bandwidth of 100 Hz at 41 kHz resonance frequency, the CRLB versus the measurement time in Eq. (12) is given by  $\sigma_f = 4.6 \times 10^{-3} \text{ Hz}^{-1/2} T_m^{-3/2}$ . The validity of the CRLB law  $\sigma_f \propto 1/T_m^{3/2}$  can be roughly estimated by comparing the amplitudes, widths and noise between two corrected spectra, for example for the two spectra in Fig. 3d, g. The amplitude ratio between Fig. 3g ( $T_m=100$  s) and Fig. 3d ( $T_m=20$  s) is 5:1, while the line-width in Fig. 3g is five times smaller compared to Fig. 3d. The total baseline noise in spectrum Fig. 3g is about 2.3 times larger compared to Fig. 3d. Therefore, the improvement in  $\sigma_f$  between the measurements shown in Fig. 3d, g is  $5(5)^{1/2} \sim 11$ , which is a first hint for the validity of the CRLB. A detailed analysis between the expected CRLB relation and the measured improvement in  $\sigma_f$  will be shown in the next section.

### 3.2 CRLB, Improvement in Measurement precision Versus Measurement Time

The measurement precision  $\sigma_f$  of a single NMR transition is a key feature of RASER NMR spectroscopy. It scales with  $\sigma_f \propto T_m^{-3/2}$  which is in stark contrast to standard NMR where  $\sigma_f \propto T_m^{-1/2}$ . How RASER NMR spectroscopy scales with  $T_m$  is visualized in Fig. 4 for two  $J$ -coupled RASER modes of  $^{15}\text{N}$ -pyridine and compared to the CRLB (green line) for reference. For the CLRb, a long-term  $\text{SNR}=12$  and a bandwidth of detection  $\text{BW}=100$  Hz are resulting in a lower bound for the precision

given by  $\sigma_f = 4.6 \times 10^{-3} \text{ Hz}^{-1/2} T_m^{-3/2}$ . In contrast to that, repetitive standard NMR measurements (red line) would only reach  $\sigma_f^{\text{NMR}} = 4.6 \times 10^{-3} \text{ Hz}^{1/2} T_m^{-1/2}$ . This proportionality factor is obtained from the uncertainty  $\sigma_f^{\text{NMR}}$  of SABRE NMR measurements, which intersects with  $\sigma_f$  of CRLB for a measurement time  $T_m = 1 \text{ s}$ .

The precision  $\sigma_f$  of both lines, shown in Fig. 4 (blue circles and black triangles), is in good agreement with the CRLB. A hypothetical CRLB assuming a tenfold improved SNR = 120 is plotted as a violet solid line. This improvement in SNR by a factor of 10 (or more) can be reached with hydrogenative PHIP instead of SABRE, generating much higher equilibrium population inversions ( $d_0 = 10^{18} - 10^{19}$ ). Such an improvement can be crucial for applications such as a sensitive two-mode RASER gyroscope. For an SNR = 12, a measurement of the earth's rotation ( $1.16 \times 10^{-5} \text{ Hz}$ , black dashed line) requires  $T_m = 60 \text{ s}$ , which could be decreased to about  $T_m = 12 \text{ s}$  or even lower with an appropriate increase in SNR.

To achieve a good RASER NMR gyroscope [36, 46–48] that can measure mechanical rotations with high precision, some conditions have to be met: (I) At least two different RASER modes are oscillating in one compartment in a common field and with sufficient spacing in frequency space. (II) The separation of the two (or more) modes are not induced by  $J$ -coupling, but are realized by different chemical shift species of the same nuclear species, or by different nuclear species such as  $^{19}\text{F}$  and  $^1\text{H}$ . (III) A sufficiently high SNR of at least 100 is realized in conjunction with very low non-common drifts of the NMR parameters. This can for example

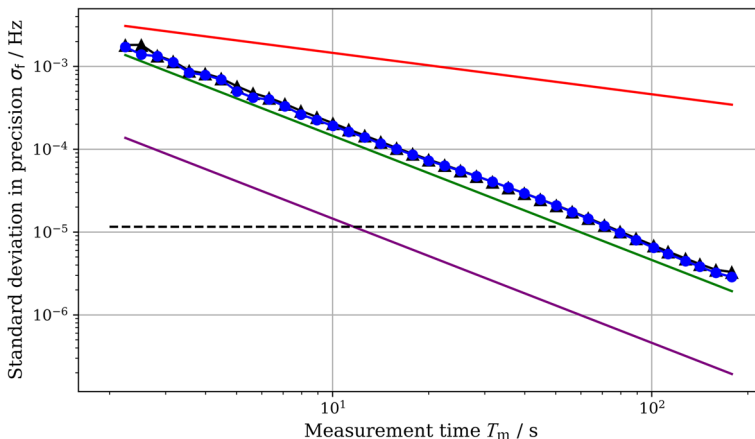


**Fig. 4** Comparison of the measured improvement of the standard deviation in measurement  $\sigma_f$  and CRLB at measurement time  $T_m$ . The green line represents CRLB for an SNR=12, given by  $\sigma_f = 4.6 \times 10^{-3} \text{ Hz}^{-1/2} T_m^{-3/2}$ . The red line represents the standard deviation of precision  $\sigma_f^{\text{NMR}} = 4.6 \times 10^{-3} \text{ Hz}^{1/2} T_m^{-1/2}$  for repeated SABRE NMR experiments. This factor is chosen such that  $\sigma_f$  intersects with  $\sigma_f^{\text{NMR}}$  for a single scan SABRE NMR measurement with  $T_m = T_2^* = 1.0 \text{ s}$ . Circles and triangles represent the measured values for  $\sigma_f$  versus time  $T_m$  for each of the  $J$ -coupled lines versus time  $T_m$ , representing the low- and high-frequency line, respectively. The dashed line indicates the earth's rotational rate, while the violet solid line corresponds to a hypothetical CRLB for a SNR = 120

be facilitated by avoiding non-common drifts for the  $^{19}\text{F}$  and  $^1\text{H}$  frequencies due to temperature variations as well as using membrane reactors [20, 49], which are less prone to fluctuations in the pumping rate. (IV) Improved hardware, including shielded ultra-low-field magnets, as well as high-Q resonators achieved by active [50] and passive [41] dedamping of the resonant circuit. V. Better measurement and optimized evaluation schemes for determining rotations, such as Kalman filtering, are employed.

### 3.3 Fluctuations and Drifts in the $J$ -coupling

Little is known about the precise dependency of the  $J$ -coupling on the temperature, the substrate concentration, or chemical surroundings. This is because the  $J$ -coupling depends weakly on these parameters. Precision measurements of the  $J$ -coupling value in the sub-mHz range could be an indicator for slight changes in molecular structure, as well as for transient molecular orbital states mediated by light or by chemical or conformational changes. First attempts to measure the  $J$ -coupling-induced splitting in the sub-mHz regime using RASER NMR spectroscopy have been reported several years ago [35]. One example is shown in Fig. 5, where the drift of the measured  $J$ -coupling-induced splitting of  $^{15}\text{N}$ -pyridine is monitored over a time period of 1200 s. A time slice with a fixed duration of 100 s corresponding to a measurement time  $T_m = 20$  s is shifted in steps of 10 s,

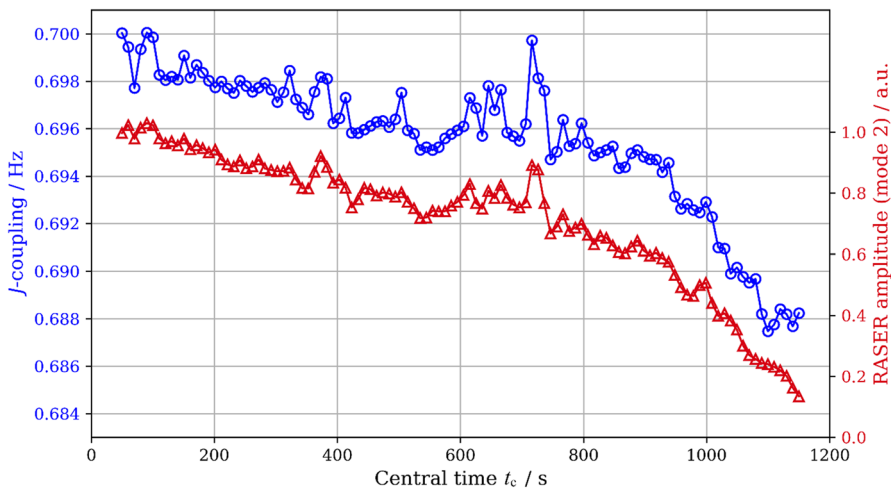


**Fig. 5**  $J$ -coupling (circles) and RASER amplitude (triangles) are plotted versus central time  $t_c$ . A window with a fixed duration of 100 s is shifted in steps of 10 s starting at  $t_c = 50$  s. This corresponds to a measurement time of  $T_m = 20$  s, as it is folded with the exponential window discussed in Sect. 2.4. At each position  $t_c$ , both  $J$ -coupled lines have been corrected for magnetic field fluctuations  $\delta B(t)$ , and the frequency difference between the two lines is evaluated. The drift of the measured line splitting correlates strongly with the RASER signal amplitude. The reasons for this behavior could be changes in population inversion  $d_0$ , as well as  $T_1$ ,  $T_2^*$  relaxation times and cavity pulling. A simulation for the drop in RASER amplitude and in  $J$ -coupling for the case of a decreasing  $T_1$  relaxation time is demonstrated in Appendix

starting at the time  $t_c = 50$  s. For each of the resulting spectra, both  $J$ -coupled lines have been corrected for magnetic field fluctuations  $\delta B(t)$  according to the procedure presented in Sect. 2.4. The result of these measurements shows slow drifts with time of about 1 mHz starting at a value of  $J = 700.0$  mHz at  $t_c = 50$  s. The observed random changes in  $J$ -coupling of about 1 mHz on the time scale of 10 s are superimposed by a continuous decrease of about 3 mHz at  $50 \leq t_c \leq 700$  s, and a steeper decrease over a range of 8 mHz for  $700 \text{ s} < t_c \leq 1150$  s. As shown in Fig. 5, both the decrease of RASER amplitude (triangles) and the observed change in splitting (circles) are remarkably correlated, even the temporary increase in  $J$ -coupling of 3.6 mHz at time  $t_c = 660$  s is reflected by the increase in the RASER amplitude. The overall trend for  $50 \text{ s} < t < 1150$  s is a continuous decrease in  $J$ -coupling by 12 mHz and in RASER amplitude by about a factor of 10. There can be various reasons for this trend. First, it could be caused by changes in the sample temperature. Second, as the bubbling with para-hydrogen causes evaporation of methanol the concentration of catalyst and of  $^{15}\text{N}$ -pyridine is increased over time. Due to a rising catalyst concentration, the  $^1\text{H}$   $T_1$  relaxation time for  $^{15}\text{N}$ -pyridine can substantially decrease. The third possible reason for a decreasing  $J$ -coupling-induced splitting is cavity pulling which occurs if the line-width  $w = 1/(\pi T_2^*)$  increases substantially with time.

In the following, we use the result of numerical simulations based on Eqs. (7–9) to narrow down the possible reasons for the correlated decay of the  $J$ -coupling-induced splitting and the RASER amplitude. The varying input parameters are a decreasing equilibrium population inversion ranging from  $8 \times 10^{16} > d_0 > 2.3 \times 10^{16}$ , or a decreasing  $T_1$  relaxation time (typically  $10 \text{ s} > T_1 > 2 \text{ s}$ ) and an increasing line-width  $0.3 \text{ Hz} < w = 1/(\pi T_2^*) < 1.2 \text{ Hz}$  as a variable input parameter.

First, we show that cavity pulling cannot explain the 12 mHz change in  $J$ -coupling-induced splitting as seen in Fig. 5. Cavity pulling attracts a given resonance line  $\nu_1$  towards the center frequency  $\nu_c$  of the cavity or of the LC-resonator. If two lines are separated in frequency by  $|\nu_2 - \nu_1|$ , and  $\nu_c \leq \nu_1 < \nu_2$ , the left line at position  $\nu_1$  is shifted towards  $\nu_c$  by a smaller amount than the right line at position  $\nu_2$ . This leads to a decrease of the observed splitting  $|\nu_2 - \nu_1|$ . To make a quantitative statement, according to [42, 43], cavity pulling is given by  $\nu_\mu^* - \nu_\mu = (\nu_c - \nu_\mu)(w/(\Delta\nu_c))$ . The observed RASER frequency  $\nu_\mu^*$  deviates from the free RASER frequency  $\nu_\mu$  by  $(\nu_c - \nu_\mu)(w/(\Delta\nu_c))$ , where  $\nu_c$  and  $\Delta\nu_c = \nu_c/Q$  are the center frequency and line-width of the LC-resonator, respectively. Given a center frequency of 41 kHz and a measured quality factor  $Q = 123$  for our setup, the bandwidth of the LC-resonator is  $\Delta\nu_c = 333$  Hz (not to be mistaken for the bandwidth of detection BW). For two RASER modes separated by a  $J$ -coupling-induced splitting of  $\nu_2 - \nu_1 = 0.7$  Hz, the relative frequency shift (the decrease in splitting  $|\nu_2 - \nu_1|$ ) due to cavity pulling is  $\delta\nu_{\text{rel}} = (w \times 0.7 \text{ Hz})/333 \text{ Hz} = 2.1 \times 10^{-3}$ . According to the simulations, a change in line-width by a factor of 2 leads to a dramatic change in the shape of the RASER signal and to multiple-period doubling, or even to chaos, in the corresponding spectrum. Period doubling and chaos will be discussed in later sections. Such strong changes over 1200 s are not observed in the

RASER signal and spectra in Fig. 3, since two isolated lines are observed over the full-time scale. In contrast to the relaxation rate  $1/T_1$ , the line-width  $w$  is mostly dominated by the inhomogeneity of the  $B_0$  field and not by the catalyst concentration. Assuming a change in the line-width  $w$  of about 50% over a time of 1100 s, which for  $T_2^* = 1$  s means a broadening from  $w = 0.318$  Hz at  $t_c = 50$  s to  $w = 0.477$  Hz at  $t_c = 1150$  s, the corresponding cavity pulling decreases the splitting from 700.0 mHz at  $t = 0$  s to 699.6 mHz at  $t = 1200$  s. This is much smaller than the measured decrease of 12 mHz over 1200 s, as shown in Fig. 5.

The simulations (see Appendix) indicate that the  $J$ -coupling induced splitting and RASER amplitude are both sensitive to changes in  $T_1$  and in  $d_0$ . In a range  $8 \times 10^{16} > d_0 > 2.3 \times 10^{16}$  and for  $10 \text{ s} > T_1 > 2 \text{ s}$ , the  $J$ -coupling induced splitting and RASER amplitude changes in the order of 25 mHz and by a factor of 10, respectively. This roughly correlates with the results shown in Fig. 5.

### 3.4 Two Gradient-Controlled RASER Modes in Individual Compartments

In this section, we discuss two RASER modes in individual compartments. When separated in this way, both modes can be pumped individually and the frequency difference can be controlled by a magnetic field gradient, when it is applied along the alignment axis of the compartments within the resonator. In this case, the mixing introduced by parahydrogen pumping collapses the frequency in both compartments into a signal line. Recently, Lohmann et al. [44] have demonstrated that multiple-period doubling, chaos or synchrony can be observed with two equal pyrazine RASER modes, depending on the gradient strength.

Here, we introduce the more general case of two chemically inequivalent RASER modes in two different compartments. The different frequencies of each compartment are realized by employing two chemically distinct RASER active species, for example acetonitrile with chemical shift  $\Delta_1 = 2.2$  ppm and a pyrazine with  $\Delta_2 = 8.5$  ppm (see Fig. 1b). At 166.6 kHz ( $B_0 = 3.9$  mT), and in the absence of a gradient ( $G_z = 0$ ), the difference in  $^1\text{H}$  RASER frequency is given by  $\nu_2 - \nu_1 = (\gamma_{\text{H}}/2\pi)B_0(\Delta_2 - \Delta_1) = 1.05$  Hz. This can be manipulated by the deliberate introduction of a gradient perpendicular to the separating slide, shown in Fig. 1b. In general, the determination of initial relaxation oscillations and the final stationary state evolution of two unequal RASER modes is fairly intricate, since, according to Eqs. (1–6), the motion has to be described in a six-dimensional space. Particularly complex behavior is expected if the radiation damping rate  $\beta d_0/\pi$  is much larger than the mode separation  $\nu_2 - \nu_1$ .

In Fig. 6a, the buildup of negative polarization with the subsequent onset of RASER activity is shown. The evolution starts at time  $t = 0$ , with the independent buildup of negative  $^1\text{H}$  spin polarization in each compartment. Due to different SABRE kinetics in the respective catalyst-substrate-complex, the pumping rates are about a factor 2–3 larger for pyrazine ( $\Gamma_2$ ) compared to acetonitrile ( $\Gamma_1$ ), ranging from  $0.05 \text{ s}^{-1} < \Gamma_2, \Gamma_1 < 0.2 \text{ s}^{-1}$ . The buildup dynamics for this SABRE activation period can be examined by a series of rf-pulses with a small tilt angle ( $\sim 20^\circ$ ). This is shown in Fig. 6a for  $0 < t < 80$  s by the series of 7 rf-pulses. A detailed view is

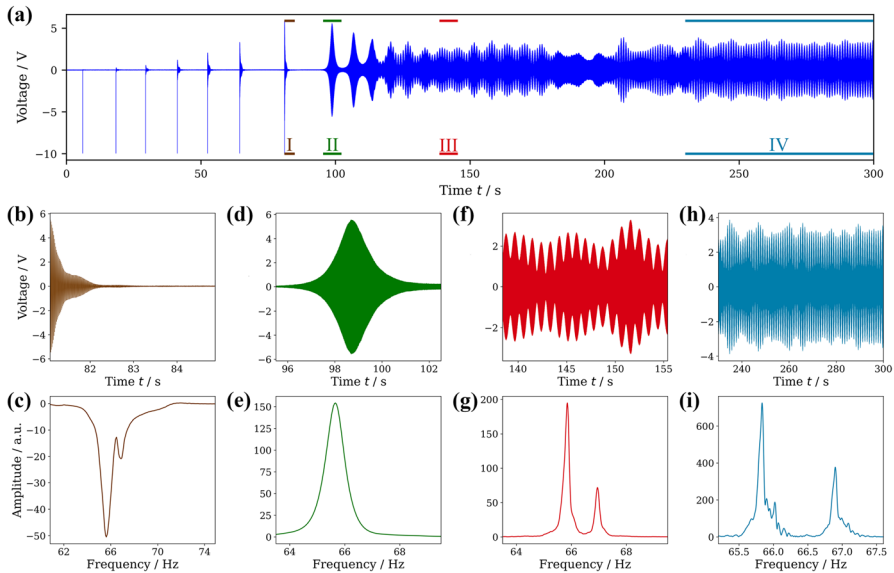


**Fig. 6** Initial SABRE polarization buildup and relaxation oscillations of the two-compartment RASER measured for pyrazine and acetonitrile. **a** Total SABRE and RASER signal evolution in the time interval  $0 < t < 300$  s after initialization of  $p\text{-H}_2$  supply. The initial RASER oscillations starting at  $t = 100$  s are diversified, with rising and disappearing periods of acetonitrile RASER action superimposed to the initial relaxation oscillation periods of pyrazine. **b** Enhanced view of the SABRE signal from window I in **a**, with the corresponding phased Fourier transformed spectrum (**c**). **d** Shows the initial RASER relaxation burst at  $t = 100$  s (window II). **e** The corresponding absolute phased spectrum shows only one RASER line at 65.7 Hz off resonance frequency, which is assigned to pyrazine. **f** At  $t = 125$  s, a beat signal appears in the RASER signal (window III). **g** The absolute phased spectrum shows both pyrazine and acetonitrile RASER lines, with an amplitude ratio of 3:1. **h** For  $230 \text{ s} < t < 300$  s (window IV), a stationary and beating RASER signal with 2.5 V amplitude can be observed. The signal is superimposed by amplitude fluctuations of about 500 mV rms, due to fluctuations of the pumping rate. **i** The corresponding absolute phased spectrum shows two-self similar structures, which indicates common field fluctuations. The spectra (**e**, **g**, **i**) were folded with an exponential window as described in Sect. 2.4 to avoid sinc artifacts

shown Fig. 6b for the largest SABRE signal (region I in Fig. 6a), just before the onset of RASER action. In the corresponding phased Fourier spectrum in Fig. 6c, two lines of unequal amplitudes separated by about 1 Hz are visible. The line having four times larger amplitude corresponds to pyrazine. They are intentionally phased to negative amplitudes, since the polarization of the SABRE pumped substrate is negative. In the phased spectrum in Fig. 6c, a faint but broad peak with positive amplitude appears, which is shifted 4.5 Hz upwards of the pyrazine reference line. This large chemical shift of about 30 ppm with respect to pyrazine is well known. It can be assigned to hydrides in the iridium complex. The broad line is in accordance with the hydrogen  $T_2$  relaxation time of about 100 ms in such a complex. The positive sign of the broad line is due to the  $J$ -coupling-induced conversion of the bound singlet state polarization into a bound triplet state with positive polarization and a negative polarization of the target protons [15]. The chemical shift difference



between the free pyrazine and acetonitrile protons is hard to measure with sufficient precision (about 1 Hz) since the two lines overlap. This changes dramatically if RASER action starts. Around  $t=100$  s, the first initial RASER relaxation oscillations can be observed. A detailed view of the first RASER burst at  $t=100$  s (region II in green) is shown in Fig. 6d. The corresponding absolute phased spectrum in Fig. 6e shows one RASER line for pyrazine, with no indication for RASER activity of acetonitrile. This changes in Fig. 6f at  $t=130$  s (region III, red), where a consistent beat of two RASER oscillations is observed. The corresponding spectrum in Fig. 6g indicates two RASER lines with 3:1 amplitude ratio, which represent pyrazine and acetonitrile. Interestingly, the acetonitrile RASER line briefly disappears again at  $t=190$  s in Fig. 6a (not shown as a spectrum). Finally, after  $t=230$  s a stationary state characterized by two stable RASER oscillations is observed in Fig. 6h. Figure 6i shows the absolute phased spectrum folded with an exponential window as defined in Sect. 2.4 over a time slice of 70 s, displaying two self-similar RASER lines with an amplitude ratio of 2:1. At first glance, this self-similarity, which is due to common field fluctuations, promises very high precision of the chemical shifts after correction of the field fluctuations. This should be similar to the previously discussed case of a  $J$ -split two-mode RASER measured in one compartment. Unfortunately, due to spatial separation both modes experience distinct dipolar field fluctuations, resulting in imperfect compensation by the correction algorithm. This will be analyzed in more detail in Sect. 3.5. Returning to the initial evolution of the RASER oscillations in Fig. 6a, we do not currently understand the fundamental origin of the large changes in the acetonitrile signal amplitude in conjunction with the initial pyrazine relaxation oscillations. A few potential factors are the interplay between the fluctuating pumping rates, different  $T_1$  relaxations rates, and the remote coupling between both species, which may exchange polarization.

### 3.5 Precision of Chemical Shift Measurement in the Two-Compartment RASER

Measuring frequency-differences in the sub-mHz regime is possible for the single-compartment RASER. The correction procedure introduced in Sect. 2.4 cancels out the common magnetic field fluctuations, including common dipolar field fluctuations. This high precision is not achievable for a two-compartment RASER with two different chemical species and two independent pumping rates. One reason for this are the non-common fluctuations of the dipole fields applying to the spatially separated compartments, which are blurring the measured chemical shift difference. According to Eq. (11) in Sect. 2.2, the angular frequency difference for  $G_z=0$  is given by  $\omega_2 - \omega_1 = \gamma_H \left[ B_0 (\Delta_2 - \Delta_1) + \delta B_{\text{dip}}^{(2)}(t) - \delta B_{\text{dip}}^{(1)}(t) \right]$ . For the two-compartment RASER in a stationary state, the fluctuations in frequency space due to non-common DDF  $(\gamma_H/2\pi) \left[ \delta B_{\text{dip}}^{(2)}(t) - \delta B_{\text{dip}}^{(1)}(t) \right]$  can be approximated by estimating the effect of the two pumping rates, which fluctuate by about 10%–20% relative to each other. To first order, this leads to relative fluctuations in the non-common DDF to an extent of about 10%–20% of the average static dipolar field in each compartment. For equal RASER amplitudes, the static dipole field in each compartment is approximately

$B_{\text{dip}}^{\text{static}} = (\mu_0/(4V_s))\hbar\gamma_H\xi d_0$ . In our two-compartment experiment, the parameters are  $\xi = -1/2$ ,  $V_s = 2 \times 10^{-7} \text{ m}^3$  and typically  $d_0 = 1.5 \times 10^{17}$ , which results in  $B_{\text{dip}}^{\text{static}} = -3.3 \text{ nT}$ . This corresponds to a static frequency shift of  $\gamma_H B_{\text{dip}}^{\text{static}} = -0.14 \text{ Hz}$  and, assuming 15% fluctuations, the expected range of frequency shifts due to non-common DDF effects is  $0.15(\gamma_H/2\pi)B_{\text{dip}}^{\text{static}} = -21 \text{ mHz}$ . Figure 7a displays a stack plot of measured RASER spectra, each of them showing two lines separated by the frequency difference  $\nu_2 - \nu_1 = (\gamma_H/2\pi)B_0(\Delta_2 - \Delta_1) = 1.05 \text{ Hz}$ . At a  $^1\text{H}$  frequency of 166.6 kHz, this corresponds to a chemical shift difference of 6.3 ppm. The left and right lines in each spectrum of Fig. 7a correspond to the chemical shift of pyrazine (8.5 ppm) and of acetonitrile (2.3 ppm), respectively. Based on the total measurement time of 300 s, 70 time slices with 80 s duration (exponential window with  $T_m = 16 \text{ s}$ , see Sect. 2.4) are created at intervals of 3.2 s. Each time slice is corrected for common field fluctuations and Fourier transformed in the absolute mode. As a result, 70 spectra are obtained, with starting times ranging from  $t_s = 0 \text{ s}$  to  $t_s = 220 \text{ s}$ . In this way, the measured frequency difference  $\nu_2 - \nu_1$  can be evaluated as a function of the starting time  $t_s$ . In Fig. 7a, all maxima in the amplitude of the left line in each spectrum are normalized to 1.0 Hz. This is due to the correction procedure and allows for an

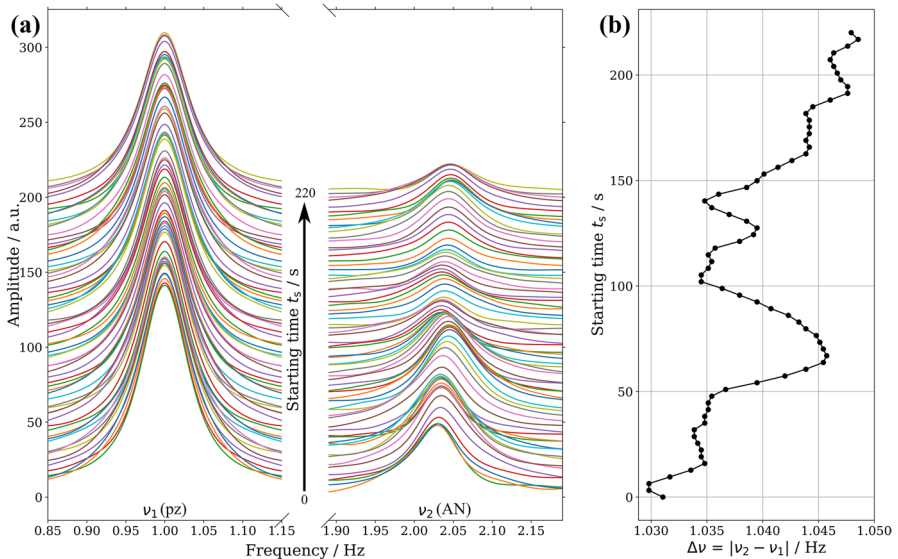


**Fig. 7** **a** Stack plot of 70 RASER spectra measured at different starting times  $0 < t_s < 220 \text{ s}$ . Each spectrum is measured at 166.6 kHz  $^1\text{H}$  resonance frequency and the time difference between successive spectra is  $\Delta t_s = 3 \text{ s}$ . The two lines correspond to pyrazine (left) at peak maximum  $\nu_1$  and to acetonitrile at peak maximum  $\nu_2$ . Both lines are corrected by common field fluctuations. The maxima of all 70 peak positions at a frequency  $\nu_1$  are shifted to 1 Hz off resonance. In this way the fluctuations of all 70 acetonitrile the peak maxima at frequency  $\nu_2$  become visible. **b** Plot of the measured frequency difference  $\nu_2 - \nu_1$  versus the starting time  $t_s$ . The precision of each measured frequency difference  $\nu_2 - \nu_1$  is about 0.5 mHz. The measured  $\nu_2 - \nu_1 = 1.04 \text{ Hz}$  on average fluctuates versus  $t_s$  by about  $\pm 10 \text{ mHz}$ . At 166.6 kHz this corresponds to a measured precision in the chemical shift difference of  $6.3 \pm 0.063 \text{ ppm}$

intuitive examination of the frequency fluctuations by observing the maximum amplitude of the right line. Figure 7b shows a magnified view of the measured frequency difference  $\nu_2 - \nu_1$  versus starting time  $t_s$ . The observed range of fluctuations in  $\nu_2 - \nu_1$  of about 20 mHz is in agreement with expectations due to non-common DDF fluctuations. These results show the current limit of precision for the measurements of chemical shift differences in an independently pumped two-compartment system to be  $6.3 \pm 0.063$  ppm. This value does not represent an absolute limit, in future the precision may be improved by two orders of magnitude if chemical shifts are measured in one chamber, with solely common field fluctuations. This was not possible in our current setup, because until now different substrates pumped by the same SABRE catalyst could not maintain RASER activity in one compartment for a sufficient long time. It seems that one chemical species is suppressed in RASER activity by the other. If this problem is solved, an opportunity arises for on-line precision measurements of different chemical species, which, unlike  $J$ -coupling, are very sensitive to small physical changes, as well as to chemical conformations and transformations.

### 3.6 The Gradient Controlled Two-Compartment RASER

Using a gradient-controlled two-compartment RASER with two separate chemical species, it is possible to alter the splitting between the two modes by applying a gradient  $G_z$ , perpendicular to the plane separating both compartments. As discussed in Sect. 2.1, the gradient-induced splitting between the two compartments is  $\nu_2 - \nu_1 = (\gamma_H/2\pi)G_z 2z_c$ . Given the distance between the two centers of gravity in each compartment as  $2z_c = 0.5$  cm, the splitting is explicitly  $\nu_2 - \nu_1 = 2.13 \text{ Hz cm mG}^{-1} \times G_z$ . A small gradient of  $G_z = -0.59$  mG/cm (including a small offset) is sufficient to compensate the chemical shift difference of 1.04 Hz. Figure 8a shows an overview of the measured splitting  $|\nu_2 - \nu_1|$  versus the gradient strength ranging from  $-2.62 \text{ mG/cm} < G_z < +1.64 \text{ mG/cm}$ . Due to the complexity of the experimental results, we proceed with a qualitative or semi-quantitative discussion.

In the range  $-0.41 \text{ mG/cm} < G_z < +1.64 \text{ mG/cm}$ , a quantitative statement is possible, since the measured  $|\nu_2 - \nu_1|$  shows a linear dependency with regard to  $G_z$ . A linear fit including ten measured points (blue circles) in this regime results in a slope of  $2.05 \text{ Hz cm mG}^{-1}$ . This is about 5% lower than the slope of  $(\gamma_H/2\pi)2z_c = 2.13 \text{ Hz cm mG}^{-1}$  expected from theory. At  $G_z = -0.65$  mG/cm, the first line collapse is observed, which means that the measured frequency difference  $|\nu_2 - \nu_1| = 0$ . This collapse into one line holds for  $-0.65 \text{ mG/cm} < G_z < -1.37 \text{ mG/cm}$ . For  $-1.37 \text{ mG/cm} > G_z$ , the line separation exceeds the collapse regime, and instead a broadened spectrum with chaotic features is observed. This chaotic regime lies in the range  $-1.37 \text{ mG/cm} < G_z < -1.92 \text{ mG/cm}$ . At  $G_z = -1.92$  mG/cm, a two-line spectrum appears again. We mention here that chaotic spectra can also be identified in the regime  $-0.65 \text{ mG/cm} < G_z < -0.41 \text{ mG/cm}$ . To exemplify the above statements, in Fig. 8b–i we present RASER signals with their corresponding absolute phased spectra. Figure 8b for  $G_z = -2.29$  mG/cm shows the beating RASER signal measured over 40 s, as well as the corresponding spectrum in Fig. 8c. The data point

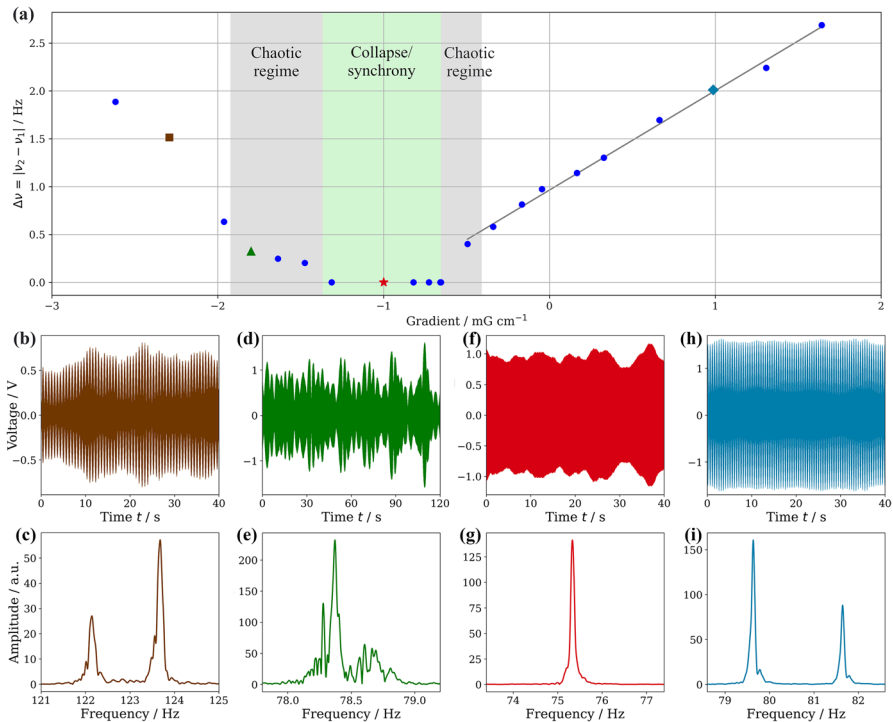


**Fig. 8** **a** Measured splitting  $\Delta\nu = |\nu_2 - \nu_1|$  in Hz versus gradient  $G_z$  in mG/cm. Three different regimes can be identified: around  $G_z = -1.0$  mG/cm (star) there is the central regime of line collapse (synchrony) ranging from  $-1.37$  mG/cm  $< G_z < -0.65$  mG/cm. The collapsed regime is embraced by two chaotic regimes ranging from  $-1.92$  mG/cm  $< G_z < -1.37$  mG/cm and from  $-0.65$  mG/cm  $< G_z < -0.41$  mG/cm. Left and right from the chaotic regimes there are two linear regimes located at  $-2.7$  mG/cm  $< G_z < -1.9$  mG/cm and  $-0.4$  mG/cm  $< G_z < +2.0$  mG/cm. Two examples for a pure two-line spectrum are indicated by a square at  $-2.3$  mG/cm and a diamond at  $+1$  mG/cm, respectively. The triangle at  $-1.9$  mG/cm stands for a chaotic spectrum. **b** Beating RASER signal and **c** corresponding two-line spectrum measured at  $-2.3$  mG/cm (square in Fig. 7a). **d** RASER signal and corresponding chaotic spectrum measured at  $-1.8$  mG/cm (triangle **a**). **f** RASER signal and **g** corresponding spectrum showing one collapsed line. **h** Beating RASER signal together with **(i)** two-line spectrum at  $1$  mG/cm (diamond in Fig. 7a)

of this gradient is identified in Fig. 8a as a square. Two lines can be identified in Fig. 8c with an amplitude ratio 1:2 and with a self-similar structure due to common field fluctuations. The smaller line on the left can be assigned to acetonitrile. In the measurement at  $-1.79$  mG/cm (indicated as triangle in Fig. 8a), the RASER signal and spectrum is measured over 120 s to achieve a sufficiently high resolution in frequency space after Fourier transformation. The signal in Fig. 8d shows a random sequence of bursts that never repeats. The corresponding spectrum in Fig. 8e is broadened, and no regular or self-similar structure can be identified. This is a

fingerprint for deterministic chaos. A proof of this claim has been recently demonstrated [44] by simulations for two interacting RASER modes. In the chaotic regime, there is an exponential divergence of close-by trajectories. For  $G_z = -1.0$  mG/cm (star in Fig. 8a), the RASER signal shown in Fig. 8f changes completely from the previously chaotic to a regular signal with typical fluctuations in the amplitude. The spectrum in Fig. 8g indicates one single collapsed line which is associated with the phenomenon of synchrony [51, 52]. Both RASER modes are oscillating at exactly the same frequency but with a phase offset. At  $G_z = +0.99$  mG/cm (diamond in Fig. 8a), the RASER signal in Fig. 8h is once again a beat signal with two well-resolved lines in the spectrum in Fig. 8i. The amplitudes ratio is now 2:1, so compared to the spectrum in (Fig. 8c) the line positions of acetonitrile and pyrazine have changed their order.

### 3.7 The Steady State ALTADENA RASER in a Halbach Magnet

In this section, we demonstrate that high-precision RASER NMR spectroscopy with field drift compensation is not restricted to low-field electromagnets in the 10 mT-regime, where typical  $^1\text{H}$  frequency drifts are about 0.4 Hz for a measurement time of 1000 s. An alternative are permanent Halbach magnets. For example, a Halbach magnet operating at 1.45 T (61.6 MHz) exhibits drifts in  $^1\text{H}$  frequency of several Hz over a time scale of tens of seconds.

Here, we discuss a steady-state RASER experiment, where the negative  $^1\text{H}$  polarization is generated outside of the Halbach magnet by PHIP in the Earth's field (ALTADENA, Adiabatic Longitudinal Transport After Dissociation Engenders Nuclear Alignment). As recently demonstrated [20, 49], an efficient parahydrogen exchange and hyperpolarization can be realized with a tube-in-tube reactor. Subsequently, the polarized sample solution is continuously transferred into the sensitive volume of the Halbach-magnet.

When hydrogenating vinyl acetate with parahydrogen under ALTADENA conditions, a continuously operating  $^1\text{H}$  RASER with two  $J$ -coupled lines separated by 7.1 Hz is obtained. Figure 9a shows an example for a  $^1\text{H}$  RASER signal of the resulting ethyl acetate measured over 26 s. An advantage of this approach is the high  $\text{SNR} = 60$  over the entire measurement time as well as relatively constant  $T_1$  and  $T_2$  relaxation times.

However, the Halbach magnet at 61.6 MHz drifts by about 5 Hz on the timescale of 26 s, which is far away from high-resolution RASER NMR spectroscopy in the sub-mHz regime. These large fluctuations are demonstrated in the corresponding absolute-mode RASER spectrum (blue) in Fig. 9b, where two self-similar blocks can be identified, each block broadened by 5 Hz and separated by about 7 Hz. The self-similarity with regular wiggles indicates a magnetic drift that changes linearly in time. After correction of the field fluctuations using an exponential window

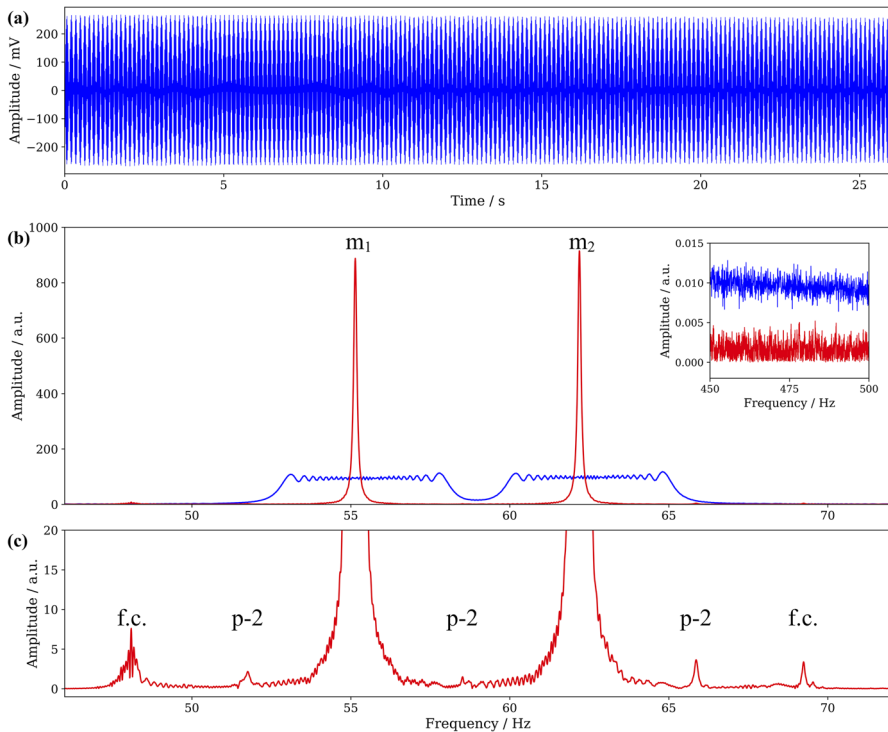


**Fig. 9** **a** Two-mode  $^1\text{H}$  RASER signal of hyperpolarized ethyl acetate [49] measured for 26 s in a 1.45 T Halbach magnet. **b** Corresponding uncorrected spectrum (blue) and corrected spectrum (red) displayed in the absolute mode. The former shows two self-similar blocks with 5 Hz width. The spectrum corrected by magnetic field fluctuations (red) contains two narrow lines at 55.140 ( $m_1$ ) and 62.189 Hz ( $m_2$ ) with linewidth  $w=0.17$  Hz and separated by  $J=7.048$  Hz. An exponential window with a measurement time  $T_m=5.2$  s is used. The precision of the measured  $J$ -coupling-induced splitting is  $\sigma_f = 2 \times 10^{-4}$  Hz. The inset in **b** shows the noise of the baselines for the uncorrected (blue) and corrected (red) spectra, both scaled to the same rms values. **c** Expanded vertical scale of the corrected spectrum from **b**. Two lines at 69.2409 and 48.069 Hz belong to a frequency comb (f.c.), while the lines at 51.758 and 58.515 and 65.859 Hz indicate a beginning period doubling process (p-2)

with  $T_m=5.2$  s, the absolute-mode RASER spectrum in Fig. 9b, red; shows two clean main lines ( $m_1$ ,  $m_2$ ) at 55.140 and 62.189 Hz, respectively, separated by  $J=7048.7 \pm 0.2$  mHz. Thus, the precision after 26 s is already in the sub-mHz regime and is expected to rise significantly in the future, as it scales with the CRLB for longer measurement times.

On top of the narrow linewidth, two other features can be observed in the corrected spectrum, as the expanded view in Fig. 9c demonstrates very small lines (about 400 times smaller compared to the main lines). First, two of these lines

are located at 48.069 and 69.2409 Hz, separated by 7.0707 Hz from the left and 7.0511 Hz from the right main lines, respectively. This is identified as a frequency comb (f.c.), which is essentially the appearance of sidebands at multiples of the frequency difference of the two main lines, caused by non-linear interactions [44]. Second, the inner three lines at 51.758 and 58.515 and 65.859 Hz are about half-way between the two main lines (58.664 Hz) and between each main line and its respective frequency comb counterpart (51.605 and 65.715 Hz). This is explained by a period-doubling process (p-2), detected in a very early stage, and not visible without correction. These results indicate that non-linear phenomena, in this case frequency comb and period-doubling, can be monitored with sub-mHz precision even in the presence of large field fluctuations. Therefore, RASER NMR spectroscopy corrected for field fluctuations is a high-precision tool for the detection of NMR parameters as well as for small non-linear effects, independent of the NMR magnet used.

## 4 Conclusion

In this contribution, we have formulated an algorithm for the correction of artifacts in RASER NMR spectra caused by common shifts, such as magnetic field fluctuations, drifts of the reference oscillator, and common DDF effects. The only necessary criterion for this algorithm to be applicable is the presence of a single, well-isolated line within the RASER spectrum to use as a reference. The algorithm has been successfully applied to the signal acquired from a single-compartment low-field (1.0 mT) RASER experiment, a two-compartment low-field experiment (3.9 mT) and a RASER in a 1.45 T Halbach magnet.

In the single compartment at a low magnetic field (1.0 mT), the obtained standard deviation in measurement precision for each line is  $\sigma_f \leq 10^{-5}$  Hz for a measurement time  $T_m \geq 60$  s. In this case, the measured improvement in precision  $\sigma_f$  versus the measurement time  $T_m$  is very close to the Cramér-Rao lower bound (CRLB) following  $\sigma_f = 4.6 \times 10^{-3} \text{ Hz}^{-1/2} T_m^{-3/2}$  over nearly four orders of magnitude ( $3 \times 10^{-6} \text{ Hz} < \sigma_f < 10^{-2} \text{ Hz}$ ). Higher SNR and operational stability in polarization build-up should bring the precision below  $10^{-6}$  Hz in the future. Observing the  $J$ -coupling-induced splitting over a time of 1200 s, we found that the changes of about 12 mHz over the entire measurement time are strongly correlated with changes of the RASER signal amplitude. Simulations based on the single-compartment two-mode RASER (see [Appendix](#)) show that this correlation can be explained by slowly decreasing  $T_1$ -relaxation time. This impedes the current precision of the measured  $J$ -coupling constant but could be alleviated by keeping the substrate and catalyst concentration stable over time.

In a two-compartment, two-substrate RASER experiment, the correction algorithm is also applicable, but the measured precision for chemical-shift differences is two orders of magnitude lower. Slight, non-common dipolar shifts between the compartments cannot be corrected by this method. Nevertheless, a significant increase in measurement precision is achieved. If the influence of non-common DDF can be reduced, the chemically shifted RASER would be a sensitive sensor towards the influence of small chemical and physical changes in the system.

We also applied a magnetic field gradient perpendicular to the separating plane of the two compartments. Just as in the two-compartment one-substrate case presented in [44], we found regimes where the spectrum contains two well-resolved lines, chaotic behavior, or a collapse. However, the transition to the collapse point was shifted to a non-zero gradient, linearly related to the chemical shift difference.

In the last section, we have extended the applicability of high-resolution RASER spectroscopy to a steady-state ALTADENA RASER that was generated in a 1.45 T Halbach magnet [49]. A precision in the sub-mHz regime for a  $J$ -coupling of ethyl acetate was achieved in a 26 s experiment, with field fluctuations over several Hz. We were also able to observe small non-linear effects, specifically a frequency comb and period doubling, which were not resolved in the uncorrected spectrum.

In summary, considering the achievable measurement precision, we envision a promising future for RASER NMR spectroscopy. This technique will strongly benefit from advances in hyperpolarization methods. While current polarization schemes are often limited to specific substances or require complex experimental procedures, efficient and universal polarization schemes would be the ideal pumping source for a RASER.

We close this contribution by motivating a gradient-controlled multi-compartment RASER, which includes different chemical species. Such a setup would constitute a sensitive quantum device with multiple available modes of operation. Potential applications range from a magnetic field or rotational sensor to a signal source producing single- or multiple frequencies or even true random noise (chaos). Additionally, the gradient-controlled multi-compartment RASER is a prototype nuclear spin-based quantum computer. Individual qubits can be realized by different frequencies (chemical shifts) in each compartment with long (or even infinitely long) decoherence times. Entanglement between two qubits can be achieved by applying a gradient, such that the frequencies between two specific compartments are collapsing, i.e. are in synchrony. According to a recent publication [53] synchrony is the classical analogue to quantum entanglement. Last but not least, understanding chaos plays an important role in stable operation involving a large number of qubits.

## Appendix

To validate the experimental results shown in Figs. 3, 4, 5 a simulation is performed, which is based on Eqs. (7–9) for two coupled RASER modes with an initial  $J$ -coupling constant of  $J=0.736$  Hz. The goal is to verify the following several essential features observed in the one-compartment RASER: (I) Simulation of noise in the



RASER signal amplitude caused by fluctuations in the pumping rate (Fig. 3). (II) Confirmation of CRLB (Eq. 12) and the measured improvement in  $\sigma_f$  under the condition of large changes in the RASER amplitude (Fig. 4). (III) Simulation of the decrease in measured RASER signal intensity, which is correlated to a drop in the observed  $J$ -coupling (Fig. 5). First, we assume a SABRE pumping rate that fluctuates by about 8% according to  $\Gamma(t) = \Gamma_0[1 + f(t)] = 0.11\text{s}^{-1}(1 + 0.08Ra(t))$ , where  $Ra(t)$  is a slowly varying random function in the interval  $[-0.5, 0.5]$  and which fluctuates with a rate  $< 1\text{ s}^{-1}$ . Second, a common random walk in frequency space of the two lines around the central frequency at  $\nu_0 = 50\text{ Hz}$  is mimicked by using the expression  $\nu_{1,2} = [50 \pm J/2]\text{ Hz} + 0.007\text{ Hz} \sqrt{t/s} Ra(t)$  in the time interval  $0 < t < 1100\text{ s}$ . Third, a slow decrease in the  $T_1$  relaxation time is assumed over the time period of 1100 s due to the evaporation of the methanol solvent. This leads to an increase in the concentration of the catalyst, which reduces the  $T_1$  relaxation time of  $^1\text{H}$  from its initial value  $T_1 = 10\text{ s}$  at  $t = 0$  to  $T_1 < 2\text{ s}$  at  $t = 1100\text{ s}$ . Similar  $T_1$  values were routinely observed in several SABRE experiments in samples with varying catalyst concentrations. The decreasing longitudinal relaxation time, given empirically by  $T_1 = 10\text{ s} [1 - 9 \times 10^{-5} (t/s)]^{1.3}$ , leads to a slow decrease in the RASER amplitude caused by an increase in RASER threshold given by  $d_{\text{th}} = (\Gamma + 1/T_1)/(\Gamma\beta T_2^*)$  [35:SI]. A slow decrease in the equilibrium population inversion  $d_0$  would have a similar effect, but we found this influence to be less significant in our case. The parameters to simulate the experimental data shown in Fig. 3a are: Angular Larmor frequency  $\omega_0 = 2\pi \cdot 41.6\text{ kHz}$ , coupling constant  $\beta = 1.13 \times 10^{-16}\text{ s}^{-1}$  (with quality factor  $Q = 100$ , filling factor  $\eta = 0.2$  and sample volume  $V_s = 4.2 \times 10^{-7}\text{ m}^3$ ), effective transverse relaxation time  $T_2^* = 1\text{ s}$  and pumping rate  $\Gamma = 0.11\text{ s}^{-1}$ . The initial conditions are: transverse spin component  $A(0) = 10^{10}$ , phases  $\phi_1 = \phi_2 = 0$  and population inversion  $d(0) = 0$ . The equilibrium population inversion  $d_0 = 8 \times 10^{16}$  at  $t = 0$  results from the total number of  $^1\text{H}$  spins (typically  $\sim 10^{19} - 10^{20}$ ) multiplied by the initial absolute polarization (typically  $10^{-3} < P_{\text{H}} < 10^{-2}$ ). The initial rate  $\beta d_0 = 9\text{ s}^{-1}$  (RASER gain) is nearly one order of magnitude above the transverse relaxation rate  $1/T_2^* = 1\text{ s}^{-1}$ , and consequently far above the initial RASER threshold  $d_{\text{th}}$ . The corresponding simulated  $^1\text{H}$  RASER signal is shown in Fig. 10a. The noise from the fluctuating pumping rate, as well as a slow decay of the RASER amplitude, is clearly visible over a time period of 1200 s. This is similar to the measured RASER signal in Fig. 3a. The expanded view for  $500\text{ s} < t < 600\text{ s}$  in Fig. 10b shows the beat signal of the two RASER modes as well as the randomly varying amplitude. The simulated RASER amplitude with the fluctuations corresponds to a signal-to-noise ratio of  $\text{SNR} = 12$ . The corresponding Fourier transformed spectrum phased in the absolute mode in Fig. 10c is characterized by two self-similar broadened peaks. The two line-structures are not exactly duplicated due to the presence of noise. The corrected spectrum in Fig. 10d is free of common magnetic field fluctuations, but the noise is still present. The result of fits to the two lines using the functions  $\text{Abs}_j(\nu)$ ,  $j = 1, 2$  (see Sect. 2.4) are indicated as a single red dashed line.

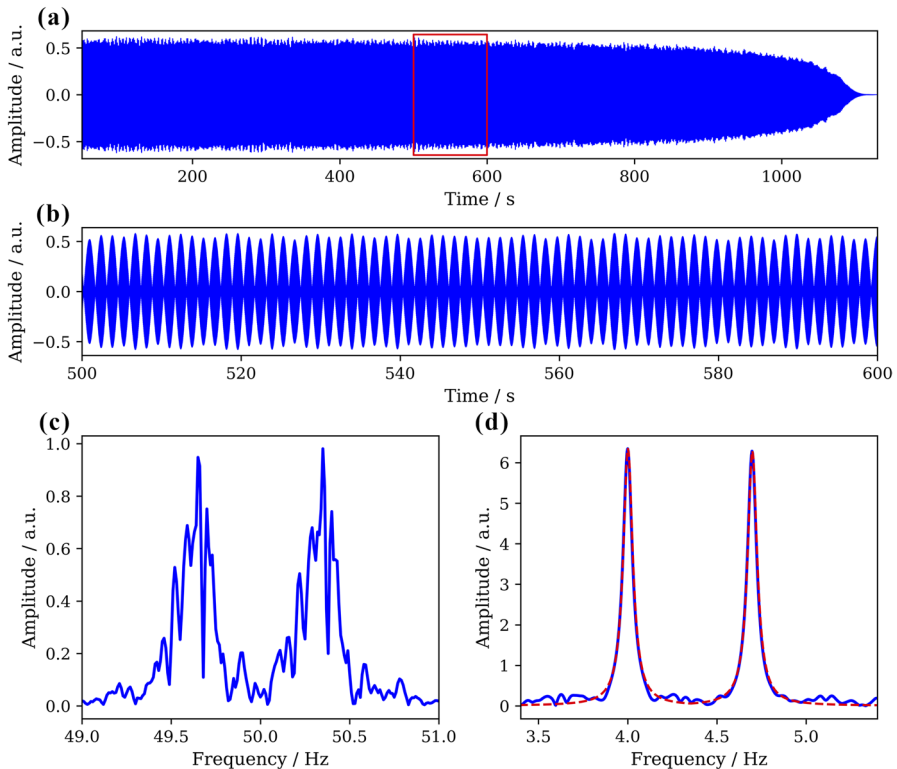


**Fig. 10** **a** Simulated single compartment  $^1\text{H}$  RASER signal, characterized by a decaying signal amplitude including 8% noise with respect to momentary amplitude. **b** The zoomed-in view for  $500\text{ s} < t < 600\text{ s}$  shows a beat pattern between the two  $J$ -coupled modes. The central time is  $t_c = 550\text{ s}$ . **c** The corresponding absolute spectrum of the signal in **b** displays two broad self-similar structures, which indicate common magnetic field fluctuations. **d** The corrected spectrum phased in the absolute mode is free of the common frequency fluctuations. The line positions  $\nu_j$ , line-widths  $w_j$  and the measurement precision  $\sigma_f$  are obtained after fitting of the absolute mode spectrum using  $\text{Abs}_j(\nu)$  with  $j = 1, 2$  as defined in Sect. 2.4

The simulated improvement in measurement precision  $\sigma_f$  versus the measurement time  $T_m$  is plotted in Fig. 11a. The values corresponding to the two lines are plotted as blue circles and black triangles, respectively. The expected improvement in precision for a  $\text{SNR} = 12$  and a bandwidth of 100 Hz is  $\sigma_f = 4.6 \times 10^{-3} \text{ Hz}^{-1/2} T_m^{-3/2}$  following CRLB (green line), and  $\sigma_f^{\text{NMR}} = 4.6 \times 10^{-3} \text{ Hz}^{1/2} T_m^{-1/2}$  for standard NMR (red line). The simulated decrease for  $\sigma_f$  (circles and triangles) is very close to the measured result in Fig. 4. In Fig. 11b, the simulated RASER amplitude (red triangles) and the  $J$ -coupling (blue circles) are plotted versus the central time  $t_c$ . Over 1100 s, the decrease in RASER amplitude by a factor of 10 is correlated to the

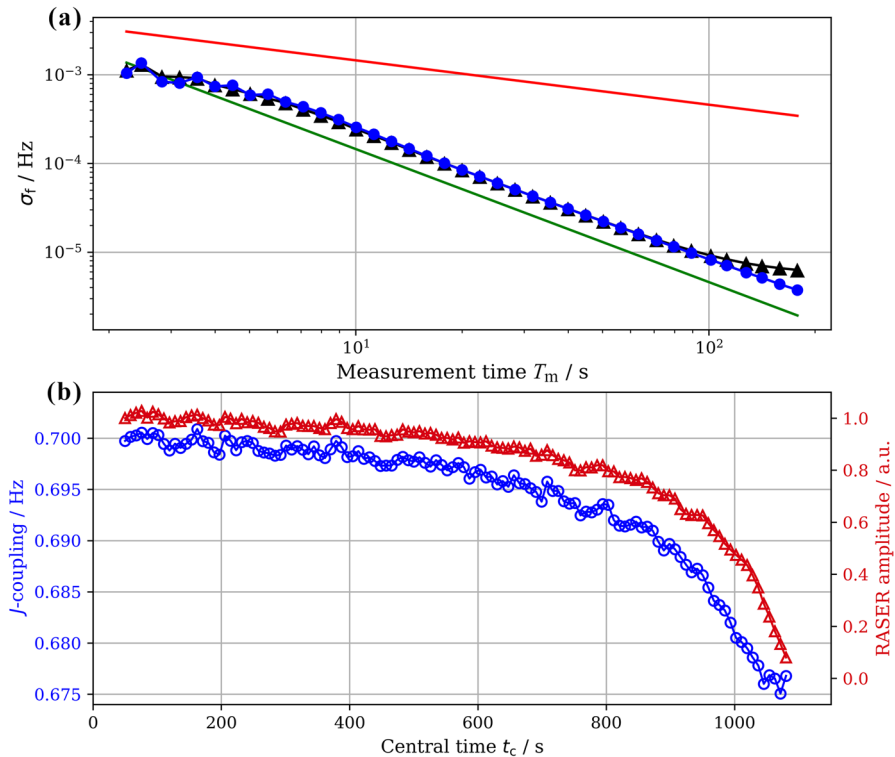


**Fig. 11** **a** Simulated decrease in measurement precision  $\sigma_f$  versus the measurement time  $T_m$ . The values closely resemble the experimental findings displayed in Fig. 4. The red and green lines correspond to the expected drop in  $\sigma_f$  for standard NMR and for the RASER, respectively. **b** Simulated decrease in RASER amplitude (red triangles) and  $J$ -coupling (blue circles) versus the central time  $t_c$ . The two curves are in good agreement with the results shown in Fig. 5

decreasing value of the  $J$ -coupling by 25 mHz. Again, this simulated decrease is in close agreement with the experimental result shown in Fig. 5.

**Acknowledgements** Stephan Appelt gratefully thanks Prof. Bernhard Blümich for his permanent support with fruitful discussions for more than 20 years. This excellent cooperation was giving the impetus for all our scientific advances and especially for building up a great friendship. Stephan Appelt acknowledges Prof. Stefan van Waasen, Prof. Astrid Lambrecht from the FZ-Jülich, and Prof. Jan Gerrit Korvink from Karlsruhe Institute of Technology for their support and the possibility of cooperation. Sören Lehmkuhl would like to thank Bernhard Blümich for entrusting him with a PhD project, always taking the time to discuss the research, and encouraging him to develop and follow his own ideas. All authors thank Jing Yang for providing the raw data of the ALTADENA RASER.

**Author Contributions** Conceptualization: SF and SA. Data curation: SF. Formal analysis: SF and SA. Funding acquisition: SA. Investigation: SF, SL, LL and SA. Methodology: SF and SA. Resources: SL and SA. Project administration: SA. Resources: SF, SL, LL and SA. Software: SF and SA. Supervision: SA.

Validation: SF, SL, SA. Visualization: SF. Writing—original draft: SA. Writing—review and editing: SF, SL and LL.

**Funding** Open Access funding enabled and organized by Projekt DEAL. Sören Lehmkuhl is supported by a YIG-Prep-Pro scholarship from KIT, funded by the Federal Ministry of Education and Research (BMBF) and the Baden-Württemberg Ministry of Science. Simon Fleischer is supported by ZEA-2 (FZ-Jülich).

**Availability of Data and Materials** The data is available from the authors upon reasonable request.

## Declarations

**Ethical Approval** Does not apply.

**Competing Interests** The authors declare no competing interests.

**Open Access** This article is licensed under a Creative Commons Attribution 4.0 International License, which permits use, sharing, adaptation, distribution and reproduction in any medium or format, as long as you give appropriate credit to the original author(s) and the source, provide a link to the Creative Commons licence, and indicate if changes were made. The images or other third party material in this article are included in the article's Creative Commons licence, unless indicated otherwise in a credit line to the material. If material is not included in the article's Creative Commons licence and your intended use is not permitted by statutory regulation or exceeds the permitted use, you will need to obtain permission directly from the copyright holder. To view a copy of this licence, visit <http://creativecommons.org/licenses/by/4.0/>.

## References

1. A.W. Overhauser, Polarization of nuclei in metals. *Phys. Rev.* **92**, 411 (1953)
2. T.R. Carver, C.P. Slichter, Experimental verification of the overhauser nuclear polarization effect. *Phys. Rev.* **102**, 975 (1956)
3. C. Griesinger, M. Bennati, H.M. Vieth, C. Luchinat, G. Parigi, P. Höfer, F. Engelke, S.J. Glaser, V. Denysenkov, T.F. Prisner, Dynamic nuclear polarization at high magnetic fields in liquids. *Prog. Nucl. Magn. Reson. Spectrosc.* **64**, 4 (2012)
4. A.J. Pell, G. Pintacuda, C.P. Grey, Paramagnetic NMR in solution and the solid state. *Prog. Nucl. Magn. Reson. Spectrosc.* **111**, 1 (2019)
5. M.A. Bouchiat, T.R. Carver, C.M. Varnum, Nuclear polarization in He<sub>3</sub> gas induced by optical pumping and dipolar exchange. *Phys. Rev. Lett.* **5**, 373 (1960)
6. W. Happer, Optical pumping. *Rev. Mod. Phys.* **44**, 169 (1972)
7. S. Appelt, A.B.-A. Baranga, C.J. Erickson, M.V. Romalis, A.R. Young, W. Happer, Theory of spin-exchange optical pumping of <sup>3</sup>He and <sup>129</sup>Xe. *Phys. Rev. A* **58**, 1412 (1998)
8. Y.-Y. Jau, T. Walker, W. Happer, *Optically pumped atoms* (John Wiley & Sons, 2010)
9. M. Batz, P.-J. Nacher, G. Tastevin, Fundamentals of Metastability Exchange Optical Pumping in Helium. *J. Phys. Conf. Ser.* **294**, 012002 (2011)
10. C.R. Bowers, D.P. Weitekamp, Transformation of symmetrization order to nuclear-spin magnetization by chemical reaction and nuclear magnetic resonance. *Phys. Rev. Lett.* **57**, 2645 (1986)
11. T.C. Eisenschmid, R.U. Kirss, P.P. Deutsch, S.I. Hommeltoft, R. Eisenberg, J. Bargon, R.G. Lawler, A.L. Balch, Para hydrogen induced polarization in hydrogenation reactions. *J. Am. Chem. Soc.* **109**, 8089 (1987)
12. C.R. Bowers, D.P. Weitekamp, Parahydrogen and synthesis allow dramatically enhanced nuclear alignment. *J. Am. Chem. Soc.* **109**, 5541 (1987)
13. J. Natterer, J. Bargon, Parahydrogen induced polarization. *Prog. Nucl. Magn. Reson. Spectrosc.* **31**, 293 (1997)

14. S.B. Duckett, C.J. Sleigh, Applications of the parahydrogen phenomenon: a chemical perspective. *Prog. Nucl. Magn. Reson. Spectrosc.* **34**, 71 (1999)
15. R.W. Adams, J.A. Aguilar, K.D. Atkinson, M.J. Cowley, P.I.P. Elliott, S.B. Duckett, G.G.R. Green, I.G. Khazal, J. López-Serrano, D.C. Williamson, Reversible interactions with para-hydrogen enhance NMR sensitivity by polarization transfer. *Science* **323**, 1708 (2009)
16. R.W. Adams, S.B. Duckett, R.A. Green, D.C. Williamson, G.G.R. Green, A theoretical basis for spontaneous polarization transfer in non-hydrogenative parahydrogen-induced polarization. *J. Chem. Phys.* **131**, 194505 (2009)
17. R.A. Green, R.W. Adams, S.B. Duckett, R.E. Mewis, D.C. Williamson, G.G.R. Green, The theory and practice of hyperpolarization in magnetic resonance using parahydrogen. *Prog. Nucl. Magn. Reson. Spectrosc.* **67**, 1 (2012)
18. T. Theis, M.L. Truong, A.M. Coffey, R.V. Shchepin, K.W. Waddell, F. Shi, B.M. Goodson, W.S. Warren, E.Y. Chekmenev, Microtesla SABRE enables 10% nitrogen-15 nuclear spin polarization. *J. Am. Chem. Soc.* **137**, 1404 (2015)
19. K.V. Kovtunov et al., Hyperpolarized NMR spectroscopy: D-DNP PHIP, and SABRE Techniques. *Chem. Asian J.* **13**, 1857 (2018)
20. P.M. TomHon, S. Han, S. Lehmkuhl, S. Appelt, E.Y. Chekmenev, M. Abolhasani, T. Theis, A versatile compact parahydrogen membrane reactor. *ChemPhysChem* **22**, 2526 (2021)
21. M.G. Richards, B.P. Cowan, M.F. Secca, K. MacHin, The 3He nuclear Zeeman maser. *J. Phys. B: At. Mol. Opt. Phys.* **21**, 665 (1988)
22. T.E. Chupp, R.J. Hoare, R.L. Walsworth, B. Wu, Spin-Exchange-pumped He 3 and Xe 129 Zeeman masers. *Phys. Rev. Lett.* **72**, 2363 (1994)
23. H. Gilles, Y. Monfort, J. Hamel, 3He maser for earth magnetic field measurement. *Rev. Sci. Instrum.* **74**, 4515 (2003)
24. D.J.-Y. Marion, G. Huber, P. Berthault, H. Desvaux, Observation of noise-triggered chaotic emissions in an NMR-maser. *ChemPhysChem* **9**, 1395 (2008)
25. A.G. Zhuravlev, V.L. Berdinskii, A.L. Buchachenko, Generation of high-frequency current by the products of a photochemical reaction. *ZhETF* **28**, 150 (1978)
26. H.-Y. Chen, Y. Lee, S. Bowen, C. Hilty, Spontaneous emission of NMR signals in hyperpolarized proton spin systems. *J. Magn. Reson.* **208**, 204 (2011)
27. A.N. Pravdivtsev, F.D. Sönnichsen, J.-B. Hövener, Continuous radio amplification by stimulated emission of radiation using parahydrogen induced polarization (PHIP-RASER) at 14 Tesla. *ChemPhysChem* **21**, 667 (2020)
28. S. Korchak, L. Kaltschnee, R. Dervisoglu, L. Andreas, C. Griesinger, S. Glöggler, Spontaneous enhancement of magnetic resonance signals using a RASER. *Angew. Chem.* **133**, 21152 (2021)
29. O.G. Salnikov, I.A. Trofimov, A.N. Pravdivtsev, K. Them, J.-B. Hövener, E.Y. Chekmenev, I.V. Koptuyug, Through-space multinuclear magnetic resonance signal enhancement induced by parahydrogen and radiofrequency amplification by stimulated emission of radiation. *Anal. Chem.* **94**, 15010 (2022)
30. P. Bösigler, E. Brun, D. Meier, Solid-state nuclear spin-flip maser pumped by dynamic nuclear polarization. *Phys. Rev. Lett.* **38**, 602 (1977)
31. D. Abergel, A. Louis-Joseph, J.-Y. Lallemand, Self-sustained maser oscillations of a large magnetization driven by a radiation damping-based electronic feedback. *J. Chem. Phys.* **116**, 7073 (2002)
32. E.M.M. Weber, D. Kurzbach, D. Abergel, A DNP-hyperpolarized solid-state water NMR MASER: observation and qualitative analysis. *Phys. Chem. Chem. Phys.* **21**, 21278 (2019)
33. M.A. Hope, S. Björgvinsdóttir, C.P. Grey, L. Emsley, A magic angle spinning activated 17O DNP raser. *J. Phys. Chem. Lett.* **12**, 345 (2021)
34. V.F.T.J. Chacko, D. Abergel, Dipolar field effects in a solid-state NMR maser pumped by dynamic nuclear polarization. *Phys. Chem. Chem. Phys.* **25**, 10392 (2023)
35. M. Suefke, S. Lehmkuhl, A. Liebisch, B. Blümich, S. Appelt, Para-hydrogen raser delivers sub-millihertz resolution in nuclear magnetic resonance. *Nature Phys* **13**, 568 (2017)
36. S. Appelt, A. Kentner, S. Lehmkuhl, B. Blümich, From LASER physics to the para-hydrogen pumped RASER. *Prog. Nucl. Magn. Reson. Spectrosc.* **114–115**, 1 (2019)
37. B. Joalland, N.M. Ariyasingha, S. Lehmkuhl, T. Theis, S. Appelt, E.Y. Chekmenev, Parahydrogen-induced radio amplification by stimulated emission of radiation. *Angew. Chem. Int. Ed.* **59**, 8654 (2020)
38. S. Appelt, S. Lehmkuhl, S. Fleischer, B. Joalland, N.M. Ariyasingha, E.Y. Chekmenev, T. Theis, SABRE and PHIP pumped RASER and the route to Chaos. *J. Magn. Reson.* **322**, 106815 (2021)

39. B. Joalland, T. Theis, S. Appelt, E.Y. Chekmenev, Background-free proton NMR spectroscopy with radiofrequency amplification by stimulated emission radiation. *Angew. Chem. Int. Ed.* **60**, 26298 (2021)
40. S. Lehmkuhl, S. Fleischer, L. Lohmann, M.S. Rosen, E.Y. Chekmenev, A. Adams, T. Theis, S. Appelt, RASER MRI: magnetic resonance images formed spontaneously exploiting cooperative nonlinear interaction. *Sci. Adv.* **8**, eabp8483 (2022)
41. M. Suefke, A. Liebisch, B. Blümich, S. Appelt, External high-quality-factor resonator tunes up nuclear magnetic resonance. *Nat. Phys.* **11**, 9 (2015)
42. C.H. Townes, 1964 nobel lecture: production of coherent radiation by atoms and molecules. *IEEE Spectr.* **2**, 30 (1965)
43. A. Winnacker, *Physik von Maser Und Laser* (Bibliograph. Inst, Mannheim, Wien, Zürich, 1984)
44. L. Lohmann, S. Lehmkuhl, S. Fleischer, M. S. Rosen, E. Y. Chekmenev, T. Theis, A. Adams, and S. Appelt, Exploring synchrony and chaos of a parahydrogen pumped two-compartment RASER. *Phys. Rev. A.* **108**, 022806 (2023)
45. S. Cavassila, S. Deval, C. Huegen, D. van Ormondt, D. Graveron-Demilly, Cramér-Rao bounds: an evaluation tool for quantitation. *NMR Biomed.* **14**, 278 (2001)
46. M. Mehring, S. Appelt, B. Menke, P. Scheufler, The physics of NMR-gyroscopes, in *High precision navigation*. ed. by K. Linkwitz, U. Hangleiter (Springer, Berlin, 1989), pp.556–570
47. T.W. Kornack, R.K. Ghosh, M.V. Romalis, Nuclear spin gyroscope based on an atomic comagnetometer. *Phys. Rev. Lett.* **95**, 230801 (2005)
48. E. A. Donley, *Nuclear magnetic resonance gyroscopes*, in *2010 IEEE sensors* (2010), pp. 17–22.
49. J. Yang, P. Wang, J.G. Korvink, J.J. Brandner, S. Lehmkuhl, The steady-state ALTADENA RASER generates continuous NMR signals. *ChemPhysChem* **24**, e202300204 (2023)
50. L. Esaki, New phenomenon in narrow germanium p–n junctions. *Phys. Rev.* **109**, 603 (1958)
51. S.H. Strogatz, From Kuramoto to Crawford: exploring the onset of synchronization in populations of coupled oscillators. *Physica D* **143**, 1 (2000)
52. S.H. Strogatz, *Nonlinear dynamics and chaos: with applications to physics, biology, chemistry, and engineering* (Avalon Publishing, 2014)
53. D. Witthaut, S. Wimberger, R. Burioni, M. Timme, Classical synchronization indicates persistent entanglement in isolated quantum systems. *Nat Commun* **8**, 14829 (2017)

**Publisher's Note** Springer Nature remains neutral with regard to jurisdictional claims in published maps and institutional affiliations.

## Authors and Affiliations

Simon Fleischer<sup>1,3</sup> · Sören Lehmkuhl<sup>2</sup> · Lars Lohmann<sup>3</sup> · Stephan Appelt<sup>1,3</sup>

✉ Simon Fleischer  
simon.fleischer@rwth-aachen.de

✉ Stephan Appelt  
st.appelt@fz-juelich.de

<sup>1</sup> Central Institute for Engineering, Electronics and Analytics-Electronic Systems (ZEA-2), Forschungszentrum Jülich GmbH, 52425 Jülich, Germany

<sup>2</sup> Institute of Microstructure Technology, Karlsruhe Institute of Technology, 76344 Eggenstein-Leopoldshafen, Germany

<sup>3</sup> Institute of Technical and Macromolecular Chemistry, RWTH Aachen University, 52056 Aachen, Germany